Effect of shape and size on the transport of floating particles on the free surface in a meandering stream

Henri R. Sanness Salmon[1], Lucia J. Baker[2], Jessica L. Kozarek[3], Filippo Coletti[1]

[1]Department of Mechanical and Process Engineering, Swiss Federal Institute of Technology (ETH), CH-8092 Zürich, Switzerland
[2]Department of Mechanical Engineering, University of Washington, Seattle, WA 98195, USA
[3]St. Anthony Falls Laboratory, University of Minnesota, Minneapolis, Minnesota, MN 55455, USA

Key Points:

- The velocity of floating particles in turbulent streams is weakly affected by their shape and size.
- Larger particles disperse faster on the free surface due to their ability to filter out small-scale turbulent fluctuations.
- Rods re-orient following the mean shear of the surface flow and rotate according to the integral scales of the free surface turbulence.

Corresponding author: Henri R. Sanness Salmon, `rsanness@ethz.ch`

Abstract

Understanding how floating particles are transported by streaming waters is crucial in predicting the transport of plastic pollution, which is dramatically abundant in rivers, lakes, and oceans. Using particle tracking velocimetry, we investigate the motion of floating particles of different shape and size on the turbulent free surface of a field-scale meandering stream. We consider two different locations, in both of which the role of surface waves on transport is deemed negligible. Millimetre-sized spheres are used as tracers to characterize the surface flow. These are compared with centimetre-sized discs and rods, approximating typical-sized pieces of floating litter. The larger particles exhibit similar mean and fluctuating velocities as the tracers but filter out the extreme turbulent accelerations. Consequently, their motion is more time-correlated and their spreading rate is larger. This behaviour is also confirmed by complementary laboratory measurements in an open channel flow. The rotation of the rods, affected by a range of turbulent scales, reduces the correlation time scale of their translational motion, and leads to a slower dispersion compared to the discs, despite the rods' length being larger than the discs' diameter. Taken together, these results indicate that the motion of finite-sized objects floating on the surface of weakly wavy turbulent waters is consistent with the behaviour of inertial particles in three-dimensional turbulence. These results can be valuable when constructing predictive models of floating plastics.

Plain Language Summary

Plastic debris is a rising global issue severely affecting the state of our rivers, lakes and oceans. Understanding how pieces of litter, often floating, travel in streaming waters is crucial for predicting and ultimately limiting plastic pollution. The main goal of this research is to investigate how the shape and size of small floating objects may affect their journey on the surface of water. To this end, we use high-speed imaging to track floating objects of different shape and size in an outdoor stream laboratory. The motion of centimetre-sized discs and rods, approximating typical pieces of plastics found in rivers, is directly compared to the motion of millimetre-sized spheres that follow the surface flow. We find that the larger discs and rods spread faster on the surface of water. Not only can these results be used to devise effective sequestration strategies, but they can be important to inform computer models that predict the abundance, and fate, of plastic litter in natural waters.

1 Introduction

Plastic debris is ubiquitous in our lakes, oceans, and coastal waters, posing a serious threat to human health and the environment (Eriksen et al., 2013; van Sebille et al., 2015; Lebreton et al., 2018). Recent findings demonstrate that about 1000 rivers account for 80 % of the global annual emissions of 0.8 to 2.7 million tons of plastics into the oceans per year, with small urban rivers among the most polluting (Meijer et al., 2021). Riverine ecosystems themselves are also affected by such pollution (van Emmerik & Schwarz, 2020). Plastic objects enter such systems in a wide range of compositions, shapes, and sizes before degrading into so-called microplastics (typically defined as pieces smaller than 5 mm). Significant efforts have been made to characterize the transport of microplastics throughout the water column (Ballent et al., 2012; H. Zhang, 2017). Several studies have explored different approaches to mitigate plastic pollution with different remediation strategies (Helinski et al., 2021; E. Zhang et al., 2022). Still, a large proportion of plastic waste in the U.S. is comprised of polyethylene and polypropylene, which are less dense than fresh water (Jambeck et al., 2015), and in general, it is estimated that more than half of all plastics produced are positively buoyant (Geyer et al., 2017). The question that motivates the present study is at which rate floating meso- and macroplastics (particles in the size range of 5 mm and larger) spread over the surface of turbulent streaming waters.

The transport of floating particles has been mainly investigated in terms of its dependence on surface waves. These impart a net drift velocity in the wave propagation direction, known as Stokes drift (van den Bremer & Breivik, 2018). While this is typically much smaller than the mean advective velocity, its magnitude increases with wave steepness and can play a role in the long-term dispersion (van Sebille et al., 2020). De Leo and Stocchino (2022) found that the wave-induced transport of negatively buoyant plastic particles is confined to a ballistic regime and a diffusive regime is rarely observed. However, the particle-to-fluid density ratio has been shown to affect the total transport by waves (Stocchino et al., 2019). While these studies have considered microplastics, mesoplastics have been shown to dwell in the near-shore regions until they degrade into microplastics which then spread offshore (Isobe et al., 2014). DiBenedetto et al. (2018, 2019) showed that non-spherical particles in wavy waters tend to follow a preferred orientation, which affects their settling velocity if those are negatively buoyant. For buoyant particles, DiBenedetto (2020) found that waves result in non-uniform particle concentration. Ultimately, to obtain a global perspective of the transport of plastics, one must also consider the effects of wind mixing, boundary currents and meteorological conditions (Ourmieres et al., 2018; Kukulka et al., 2012).

The nature of turbulence of the free surface is still debated. Pan and Banerjee (1995) identified hallmark features such as upwelling and downwelling motions and long-lived vortices. Kumar et al. (1998) measured a k^{-3} decay of the velocity spectra (k being the wavenumber), consistent with the expectation for two-dimensional (2D) turbulence. On the other hand, the field measurements of Chickadel et al. (2011) displayed a $k^{-5/3}$ behaviour typical of three-dimensional (3D) turbulence. In the riverine environment, the shallowness of the flow plays a significant role in determining the nature of the turbulence: in particular, in the presence of strong lateral shear, the limited depth inhibits vortex stretching and may result in vortex dynamics akin to 2D-turbulence, especially at low wavenumbers (Uijttewaal & Booij, 2000). Most previous studies focused on free surface turbulence have been concerned with the topological features of the flow, often in relation to air-water gas fluxes (Shen et al., 1999; Shen & Yue, 2001; McKenna & McGillis, 2004; Turney & Banerjee, 2013; Herlina & Wissink, 2014), with only a few studies concerned with the transport of particles on it. Particularly, Cressman et al. (2004) and Lovecchio et al. (2013) found that tracer particles floating on the free surface cluster into string-like structures with long lifetimes. Characteristic features of shallow flows, such as transitional macro-vortices, have been found to greatly affect the single-particle and particle-pair dispersion (Stocchino et al., 2011).

Several field studies have been concerned with natural free surface flows, focusing on the effectiveness of free surface velocity measurements (e.g., for discharge estimation as well as flow monitoring during flood events). The methods include acoustic Doppler velocimetry (ADV) but also imaging techniques originally developed for laboratory flow studies, such as particle image velocimetry (PIV) and particle tracking velocimetry (PTV) (Raffel et al., 2018; Adrian & Westerweel, 2011). Free surface PIV and PTV present technical challenges even in laboratory studies: the choice of appropriate tracers and their successful imaging in spite of surface reflections (Weitbrecht et al., 2002; Miozzi et al., 2010; Miozzi & Romano, 2020; Gomit et al., 2022). These difficulties are exacerbated in field studies due to uneven natural illumination and scarcity of detectable floating tracers. Nevertheless, these techniques have gained favour in riverine flow investigations due to the richness of the data they can provide (Jin & Liao, 2019; Tauro et al., 2016, 2019). Recent studies regarding floating debris have shown the importance of surface tension and how it can play a key role in the transport of partially submerged floating macroplastics, as its effects can be of the same order or magnitude as buoyancy and turbulence (Valero et al., 2022).

Here we investigate experimentally the motion of floating particles on the turbulent free surface of a meandering stream in an outdoor facility which offers laboratory-quality measurements, and control, in a field-scale setting. We focus on regimes in the absence of wind where the amplitudes of, and the drift induced by, surface waves are too small to

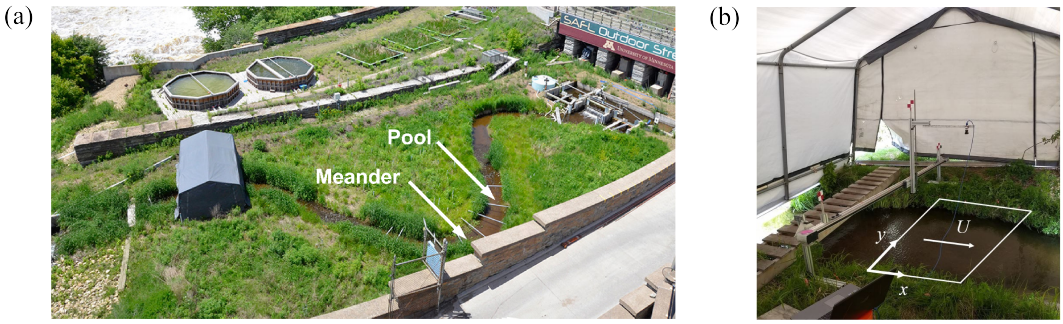

Figure 1. (a) The OSL facility, with the locations of the two ROIs (meander and pool) indicated by arrows. The tent, shown here at a downstream location, is deployed over the ROIs in the present experiments. (b) The traversing system holding the camera used for free surface imaging, indicating the approximate location of the FOV in the meander and the 2D coordinate system.

appreciably modify the advective transport. The main goal of the study is to explore the influence of the shape and size of floating particles along their trajectories when driven by the multi-scale fluctuations of the free surface flow. The focus is on size ranges relevant to meso- and macroplastics ($\geq 5\,\mathrm{mm}$) which are highly relevant to but largely understudied in river flows (van Emmerik & Schwarz, 2020). Applying time-resolved PTV to millimetre-sized spheres, we obtain surface velocity fields at two different locations along the stream. We then characterize the transport of centimetre-sized discs and rods and directly compare them to the behaviour of the spheres. In particular, we examine the floating particles' response to the free surface turbulent fluctuations which in turn affects their spreading rate. The observed behaviours are confirmed in well-controlled laboratory experiments, indicating the findings hold beyond the specific field settings. The rotational dynamics of the rods is considered to gain insight on their dispersion as compared to the discs. As we will discuss, the sensitivity of the particle dispersion to small-scale turbulence may have important consequences for modelling approaches based on flow velocity data (which are necessarily coarse-grained in space and time).

2 Materials and Methods

2.1 Field-scale Stream Facility and Hydrodynamic Characterization

Measurements are performed in the Outdoor StreamLab (OSL), an outdoor field-scale experimental stream facility at the Saint Anthony Falls Laboratory, University of Minnesota (Figure 1a). Water is drawn from the Mississippi River, flows through a meandering channel and discharges back into the river. The flow rate is controlled via a valve at the inlet, and the incoming water flows into a headbox and over a weir before entering the channel. The monitoring of the water height at the weir allows real-time calculation of the flow rate Q. Two flow rates are considered, $Q_1 = 32.1\,\mathrm{L\,s^{-1}}$ and $Q_2 = 53.7\,\mathrm{L\,s^{-1}}$, for which transport of sediment is negligible and the river bed is static. A Massa M300 ultrasonic distance probe and a sonar transducer are mounted on a programmable measurement carriage, performing 2D elevation scans of the water surface and channel bed. Measurements are acquired in two regions of interest (ROI): one located at one of the meanders in the stream, and the other over a scour pool downstream of a riffle. We will refer to these measurement locations as the meander and the pool, respectively. The riverbanks can affect significantly the transport of particles (van Emmerik & Schwarz, 2020). In the present experiments, we have not focused on this aspect and rather investigated the interaction of floating particles on the turbulent free surface. Therefore, to minimize interaction with the bank, vegetation along it was either trimmed away or pinned down to avoid particle entrapment.

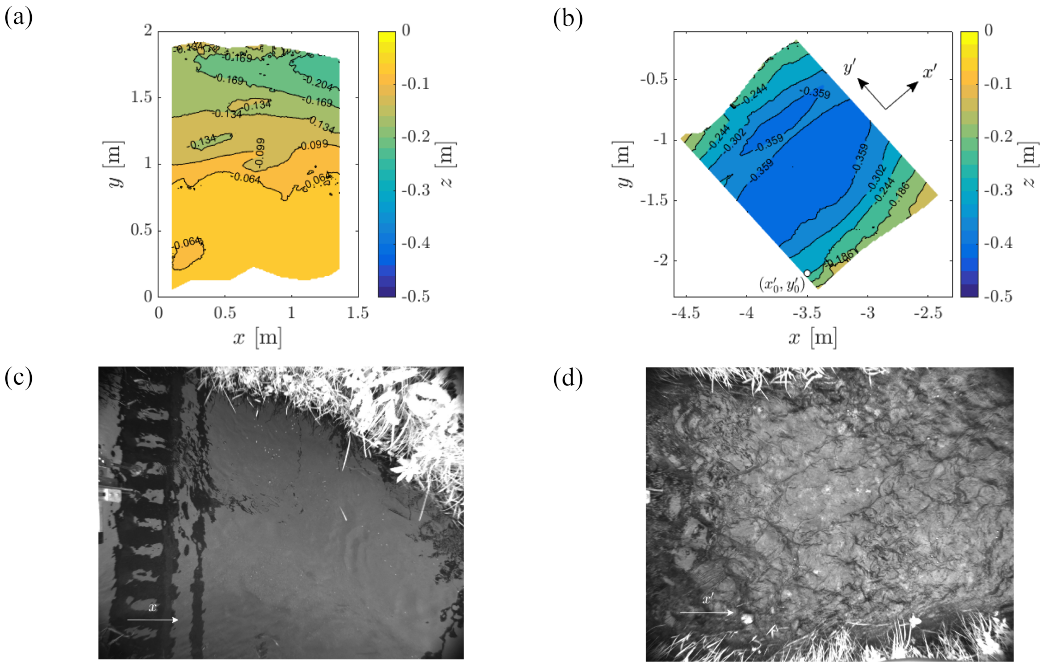

Figure 2. Bathymetry of the meander (a) and the pool (b) for Q_2. The origin of the alternative coordinate system for the pool (x_0', y_0') and the directions of the abscissa and ordinate are indicated. Instantaneous photographs of the free surface at the meander (c) and the pool (d) for the same flow rate, indicating the streamwise direction x and x', respectively.

The bathymetries of both ROIs are shown in Figure 2a-b. The origin of the global coordinate system is chosen to be on the bank of the meander, with x approximately in the streamwise direction, y pointing from the inner to the outer bank, and $z = 0$ m corresponding to the water surface. At the pool we also define an additional coordinate system x'-y', with origin $(x_0', y_0') = [-3.5, -2.2]$ m and x' approximately aligned with the local flow direction.

The near- and sub-surface flow velocity $\vec{u}(\vec{x}, t)$ is also characterized by a Nortek Vectrino ADV probe, traversed along the cross-sections at $x = 1$ m and $x' = 1$ m in the meander and the pool, respectively. The phase-space thresholding technique described in Parsheh et al. (2010) is used to remove occasional spurious velocity spikes (e.g. due to air bubbles). Measurements are acquired at 100 Hz for 120 s. In the meander 24 and 27 locations are sampled along the cross-section for Q_1 and Q_2, respectively. Correspondingly, 21 locations are sampled in the pool for both flow rates.

The hydrodynamic conditions of both ROIs are summarized in Table 1. The Reynolds number $\mathrm{Re} = HU_b/\nu$ and the Froude number $\mathrm{Fr} = U_b/\sqrt{gH}$ are based on the water depth H and the bulk flow velocity U_b, both spatially averaged over the respective ROIs. Here, $U_b = Q/A$ is calculated from the cross-sectional area A inferred from the bathymetry, g is the gravitational acceleration, and ν is the fluid kinematic viscosity. Despite the meander being shallower and associated with a larger Fr, the pool displays a wavier surface (Figure 2c-d) which is attributed to the turbulence induced by the rocky bed of the riffle upstream of this region (Brocchini & Peregrine, 2001). In both ROIs $\mathrm{Fr} \ll 1$, and indeed the ultrasonic probe data indicates limited deformation of the free surface: the root mean square (RMS) fluctuations of the water surface level are approximately 1 mm and 2 mm in the meander and the pool, respectively, which provide an estimate of the wave amplitude a. Instantaneous images (acquired as described below) indicate wavelengths λ of 3 to 6 cm in the meander and 4 to 8 cm in the pool. To obtain first-order estimates of the wave effect on the floating

Table 1. Main hydrodynamic parameters of the meander and the pool for both flow rates Q: mean depth of the channel H, mean width of the channel B, mean cross-sectional area A, bulk fluid velocity U_b, Reynolds number Re, and Froude number Fr.

Meander	H [m]	B [m]	A [m^2]	U_b [m s^{-1}]	Re	Fr
$Q_1 = 32.1$ L s^{-1}	0.08	1.72	0.143	0.225	18,480	0.25
$Q_2 = 53.7$ L s^{-1}	0.10	—	0.177	0.303	30,910	0.30
Pool	H [m]	B [m]	A [m^2]	U_b [m s^{-1}]	Re	Fr
$Q_1 = 32.1$ L s^{-1}	0.29	1.68	0.492	0.065	18,977	0.04
$Q_2 = 53.7$ L s^{-1}	0.31	—	0.525	0.102	31,750	0.06

Table 2. Main properties of the floating particles: material, particle-to-fluid density ratio ρ_p/ρ, equatorial radius a, polar radius c, and aspect ratio λ.

Particle Type	Material	ρ_p/ρ	a [mm]	c [mm]	λ
Spheres	Polypropylene	0.9	2.5	2.5	1.00
Discs	Softwood	0.75	19.1	1.6	0.08
Rods	Softwood	0.75	0.9	31.8	35.28

particle transport, we use relations for monochromatic surface waves (Lighthill, 2001). The maximum horizontal velocity of a floating particle due to the wave field is the maximum orbital velocity Sc_p, where $S = ak$ is the wave slope, $k = 2\pi/\lambda$ is the wavenumber and $c_p = \sqrt{gk}$ is the deep-water phase velocity. This yields around $0.03\,\mathrm{m\,s^{-1}}$ and $0.05\,\mathrm{m\,s^{-1}}$ for the meander and pool, respectively, which are small compared to the measured free surface velocities. Consistent with this estimate, Del Grosso et al. (2019) reported RMS free surface velocities induced by gravity-capillary waves of a few $\mathrm{cm\,s^{-1}}$, but for waves with much larger amplitude and similar slope. In conclusion, while the wave-induced surface motion may participate to the transport, it is not expected to majorly affect our conclusions.

2.2 Floating Particles

Three types of floating particles are used in the present experiments. White polypropylene beanbag filler pellets, approximately spherical with a 5 mm diameter, are used to characterize the surface flow velocity. These are sufficiently large to be accurately detected by imaging and can be recaptured downstream of the ROIs. To explore the effect of shape and size on particle transport, larger centimetre-sized discs and rods are utilized. The discs consist of wooden craft circles and the rods are wooden toothpicks, both spray-painted white to increase their visibility and to reduce the absorption of water.

When describing non-spherical particles in turbulence such as discs and rods, it is common to idealize their shape as spheroids. Any spheroid can be specified by its aspect ratio $\lambda = c/a$, defined as the ratio between the polar radius c (i.e., the length of the semi-axis perpendicular to the plane of symmetry) and the equatorial radius a (i.e., the length of the semi-axis along the plane of symmetry): $\lambda = 1$ is a sphere, $\lambda < 1$ is an oblate spheroid (disc), and $\lambda > 1$ is a prolate spheroid (rod). The different particle properties are summarized in Table 2.

2.3 Particle Response Time

When assessing the ability of particles to follow the fluid velocity fluctuations it is customary to quantify the Stokes number $\mathrm{St} = \tau_p/\tau_f$, where τ_p is the particle response time and τ_f is a relevant time scale of the flow. The latter is usually taken as the Kolmogorov time scale τ_η (the time scale of the smallest turbulent eddies), due to the significance of the particle interaction with the microscale structure of the turbulence (Wang & Maxey, 1993; Balachandar & Eaton, 2010; Brandt & Coletti, 2022). While the dynamics of free surface turbulence is not fully understood and the applicability of Kolmogorov theory is debated (Hunt & Graham, 1978; Magnaudet, 2003), experimental and numerical studies have documented a $k^{-5/3}$ scaling of the energy spectra at or near the free surface (Chickadel et al., 2011; Flores et al., 2017). As we will show, both the near-surface ADV measurements and the PTV measurements confirm such a scaling in the present setting, allowing us to estimate τ_η (see Section 3.2). Evaluating τ_p of floating particles, however, is especially challenging. This is usually defined as the characteristic time over which a particle responds to changes in the surrounding fluid velocity through the drag force. The latter depends on the level of submergence (Beron-Vera et al., 2019), which is not accurately known for particles floating in turbulent flows and cannot be accurately measured here. Alternatively, τ_p can be defined as the integral, over time, of the particle acceleration autocorrelation. However, measuring this reliably requires a spatio-temporal resolution hardly achievable in a large-scale outdoor setting, and beyond the capability of the present imaging system. Therefore, in the following, leveraging previous studies of finite-size particles in turbulence, we opt for an estimate of St based on the size of the particles compared to the Kolmogorov scale η (the size of the smallest free surface turbulent eddies, see Section 3.2).

Laboratory experiments from Fiabane et al. (2012) and particle-resolved simulations from Homann and Bec (2010) and Uhlmann and Chouippe (2017) indicate that spherical particles in turbulence behave as tracers up to $d_p \sim 5\eta$; while larger particles have a Stokes number that approximately scales as $\mathrm{St} = \tau_p/\tau_\eta \sim 1 + 0.08 d_p/\eta$. Homann and Bec (2010) argued for a power-law dependence $\propto (d_p/\eta)^{2/3}$, but the quantitative outcome is similar. As we will see, $\eta \approx 0.5$ mm in the meander, thus, $d_p/\eta \sim 10$ (i.e., $\mathrm{St} \sim 2$) for the spheres. While the spheres may not respond faithfully to the smallest-scale fluctuations, they are expected to capture most of the turbulent kinetic energy, to first-order accuracy, being 30 to 50 times smaller than the energy-containing turbulent eddies of size L. As a result, we will regard them as tracers of large-scale motions. This is consistent with Nikora et al. (2007), where 3 mm floating particles were deemed suitable tracers for free surface turbulence in a laboratory flume. For non-spherical particles, the estimation of τ_p is even more complex due to their geometry. Considering the length of maximum extension, $2a$ for the discs and $2c$ for the rods, we estimate $\mathrm{St} \approx 9$ and 14, respectively. The elongated shape of the rods, however, suggests that alternative measures of their effective size (e.g., the volume-equivalent diameter) may be more suitable. In general, the larger particles are expected to have significantly longer response times than the mm-sized spheres.

In the pool, we lack precise estimates of the Kolmogorov scales; as the turbulence intensity and so the dissipation rate is higher, η is expected to be somewhat smaller, hence St may be accordingly larger yet comparable to the levels in the meander. As we will discuss, the observed behaviour of the larger particles is consistent with such estimates. We shall remark that St is not a sufficient parameter to characterize the behaviour of finite-sized particles in turbulence (Lucci et al., 2010). The present estimates are solely meant to guide in the later phenomenological interpretation of the results.

2.4 Particle Imaging and Tracking

A 1 Mpx CMOS camera (Allied Vision Mako U-130B) with a 3 mm wide-angle lens is mounted on a cantilever arm attached to a traversing system composed of aluminum beams (Figure 1b). The camera is suspended 1.5 m above the water surface, imaging a $2.2\,\mathrm{m} \times 1.7\,\mathrm{m}$

field of view (FOV). As it will be shown, for both considered locations, this is much larger than the integral scale of turbulence L. To minimize reflections on the water surface, a large tent is set up to enclose the camera and the FOV, blocking direct sunlight that would cause reflections and any wind that may affect the free surface.

The particles are dispensed using a bin spanning the width of the channel, ensuring a nearly homogeneous particle distribution, and retrieved via a nylon seine net at the downstream end of the stream. The camera records at a frame rate of 30 to 50 Hz depending on the ROI and Q, keeping the inter-frame particle displacement to about 6 pixels. For each flow rate case and each ROI, measurements are performed over four separate runs to prevent the net from filling with particles and obstructing the water flow. Each run contains about 15 000 to 20 000 images. In total, this yields approximately 16 000 particle trajectories for the spheres and 1000 trajectories for the discs and rods. We verify that each of the four runs per particle type yields the same quantitative results for each flow rate, thus statistical uncertainty due to finite sample size does not affect the conclusions.

The wide-angle camera lens introduces some image distortion. To correct it, a $0.9\,\mathrm{m} \times 1.2\,\mathrm{m}$ checkerboard pattern is imaged at the same distance as the water surface, and the appropriate de-warping transform is determined (Z. Zhang, 2000). Despite the tent blocking direct sunlight, some glare off the water surface from the diffused ambient light is still present. This time-dependent background noise is removed using the proper orthogonal decomposition (POD)-based method by Mendez et al. (2017), which isolates the modes mostly contributing to the intensity variance of the images. We subtract the first two modes, which successfully removes most of the glare while preserving the particles in the images.

Particles are identified by employing threshold-based image segmentation (i.e., finding continuous groups of pixels exceeding an intensity threshold). The probability distribution function (*p.d.f.*) of the areas of these groups of pixels is considered, and a rejection criterion is set at ± 2 standard deviations from the expected value based on the pixel/mm ratio. Particle trajectories $\vec{x}_p(t)$ are formed using a custom-written nearest-neighbour PTV algorithm (Baker & Coletti, 2019, 2021, 2022), and their velocities $\vec{u}(\vec{x}_p(t))$ and accelerations $\vec{a}(\vec{x}_p(t))$ are obtained by convolution with the first and second derivative of a Gaussian kernel in the time domain, respectively. A temporal kernel $t_k = 16$ frames is chosen as the smallest value beyond which the total acceleration variance σ_a^2 decays exponentially (Figure 3a). This approach has been used in several previous laboratory and field studies (Voth et al., 2002; Nemes et al., 2017; Li et al., 2022; Berk & Coletti, 2021; Baker & Coletti, 2021, 2022). We also characterize the rods' orientation and rotation rate along their trajectory. The orientation is defined by the unit vector $\hat{p}$ aligned with the rod's symmetry axis, obtained from an ellipse best-fit to the valid pixel groups. The angular velocity $\Omega(t)$ is obtained by convolving $\hat{p}(t)$ with the first derivative of a Gaussian kernel, analogous to the particle velocity using the same t_k.

2.5 Laboratory Water Channel

To complement the study in the OSL, laboratory experiments on particles floating in turbulent water are conducted at ETH Zürich (Figure 4). A recirculating open channel is used, with a $0.5\,\mathrm{m} \times 0.5\,\mathrm{m} \times 2.0\,\mathrm{m}$ test section. The water depth is 0.4 m and a bulk velocity $U_b = 0.24\,\mathrm{m\,s^{-1}}$ is imposed by a centrifugal pump. Turbulence is generated by a square-mesh grid inserted at the inlet of the test section, with mesh size $M = 35\,\mathrm{mm}$ yielding a Reynolds number $\mathrm{Re}_M = MU_b/\nu = 8400$. With a Froude number $\mathrm{Fr} = 0.12$, the water surface is weakly deformed by waves with amplitude smaller than 0.5 mm. To characterize the free surface turbulence 2 mm polyethylene spheres (Cospheric LLC) are used. These are around 5 times larger than η thus sufficiently small to be considered effective tracers. To investigate the effect of particle size, discs of 5 mm and 10 mm in diameter, laser cut out of 1 mm thick polypropylene sheets, are utilized. A nylon net is placed at the outlet of the test

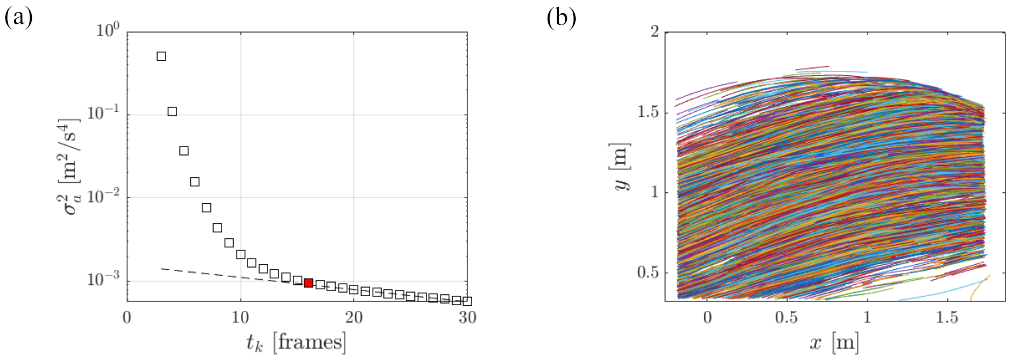

Figure 3. (a) Total particle acceleration variance plotted against the Gaussian smoothing kernel size for the spheres in the meander for Q_1. The filled data point corresponds to the chosen kernel size for this data set and the dashed line represents the exponential decay of the acceleration variance. (b) 1% of the respective smoothed particle trajectories, drawn with different colours for visualization purposes.

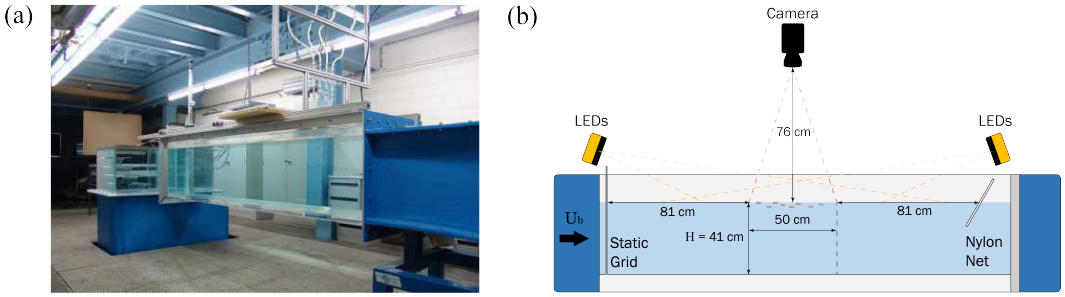

Figure 4. (a) The large recirculating water channel operated at ETH Zürich. (b) The experimental imaging setup.

section to recapture the particles. A 0.45 m × 0.5 m FOV is imaged via a 12 Mpx CMOS camera (Baumer VQXT-120C.HS) operated at 90 Hz with a 35 mm lens. The upstream edge of the FOV is located 0.81 m from the grid, which is sufficient for the turbulence to have reached equilibrium conditions (Hearst & Lavoie, 2014). The particles are illuminated by a pair of continuous LED lights. Their centroids are obtained via threshold-based image segmentation followed by a circle-finder routine. The trajectories are reconstructed using the same PTV algorithm as described above for the outdoor stream measurements. At least 10 000 trajectories per particle type are acquired.

3 Results and discussion

3.1 ADV Measurements

We first consider the ADV measurements to assess the near- and sub-surface flow in the ROIs. Figure 5 shows the temporal mean and RMS fluctuations of the streamwise velocities for the meander (a-b) and the pool (c-d). Measurements are shown for one flow rate in each ROI, the trends being analogous for both considered flow rates. In the meander, horizontal near-surface velocity averaged over the ROI is $\langle \vec{u} \rangle = [0.30, 0.07]$ m s^{-1} and $\langle \vec{u} \rangle = [0.34, 0.05]$ m s^{-1} for Q_1 and Q_2, respectively. The nonzero spanwise velocity is expected for a curved section of a natural stream. Conversely, the pool displays weak spanwise velocity

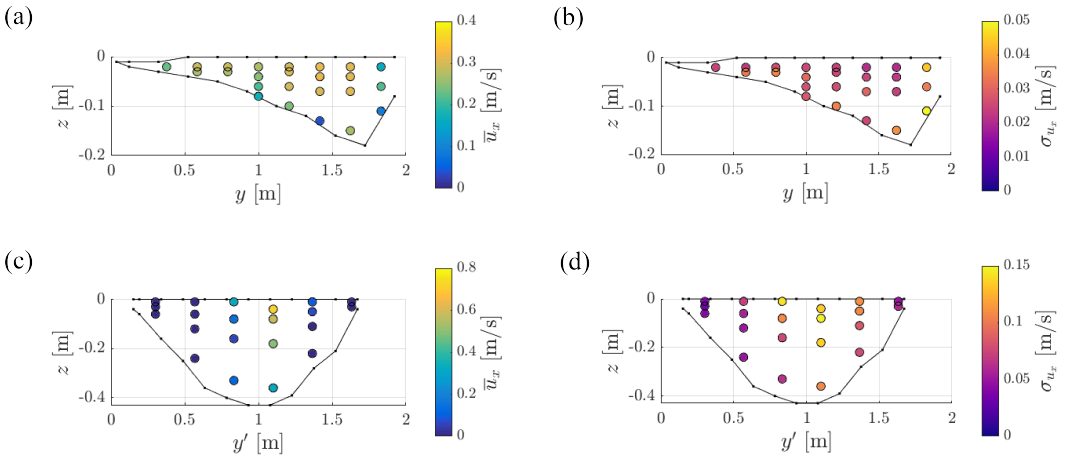

Figure 5. The temporal mean (a) and RMS fluctuations (b) of the streamwise velocity in the meander, measured by ADV, at various points along the cross-section at $x = 1\,\mathrm{m}$ for Q_1. The temporal mean (c) and RMS fluctuations (d) of the streamwise velocity in the pool, measured by ADV, at various points along the cross-section at $x' = 1\,\mathrm{m}$ for Q_2.

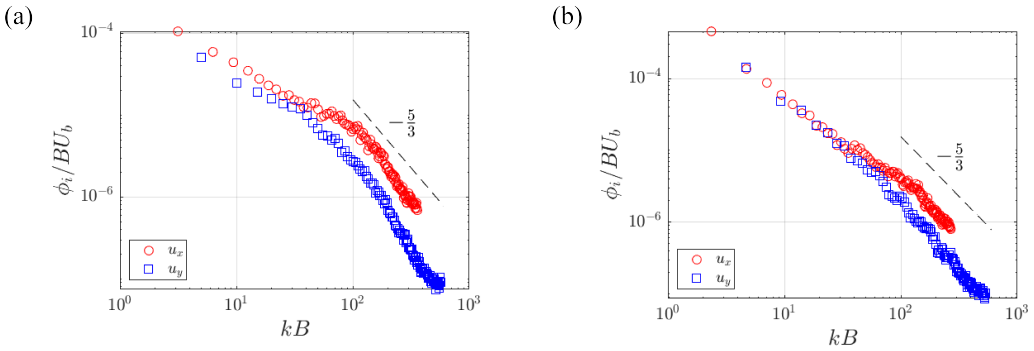

Figure 6. Normalized power spectral densities of the near-surface ADV measurements taken in the meander at $\vec{x} = [1, 1, -0.02]$ m for Q_1 (a) and Q_2 (b). The dashed line corresponds to $k^{-5/3}$ scaling.

and high streamwise velocity along the midline. This indicates a jet-like flow structure, bounded by shear layers which are associated with high-velocity fluctuations. This view will be confirmed by the free surface flow imaging. Furthermore, the flow in the meander displays significant turbulence intensity throughout the water column, with streamwise RMS fluctuations exceeding 10 % of U_b. Figure 6 shows the normalized power spectral density of the near-surface velocity fluctuations measured 2 cm below the water surface. We recover the classic $k^{-5/3}$ scaling for the streamwise and spanwise components of the free surface velocity over a sizeable range of wavenumbers.

3.2 Free Surface Flow Characterization

We consider the Eulerian fields of the mean velocity $\tilde{U}(\vec{x})$, and the RMS fluctuations $\sigma_U(\vec{x})$, where $U = \sqrt{\vec{u}(t) \cdot \vec{u}(t)}$ is the norm of the particle velocity vector. The Eulerian data is obtained by binning the trajectories into fixed interrogation windows of 5 cm × 5 cm. This allows for a temporal averaging of at least 25 instantaneous vectors in each window and is indicated by $\tilde{\cdot}$. The results for both measurement locations for Q_1 are shown in Figure

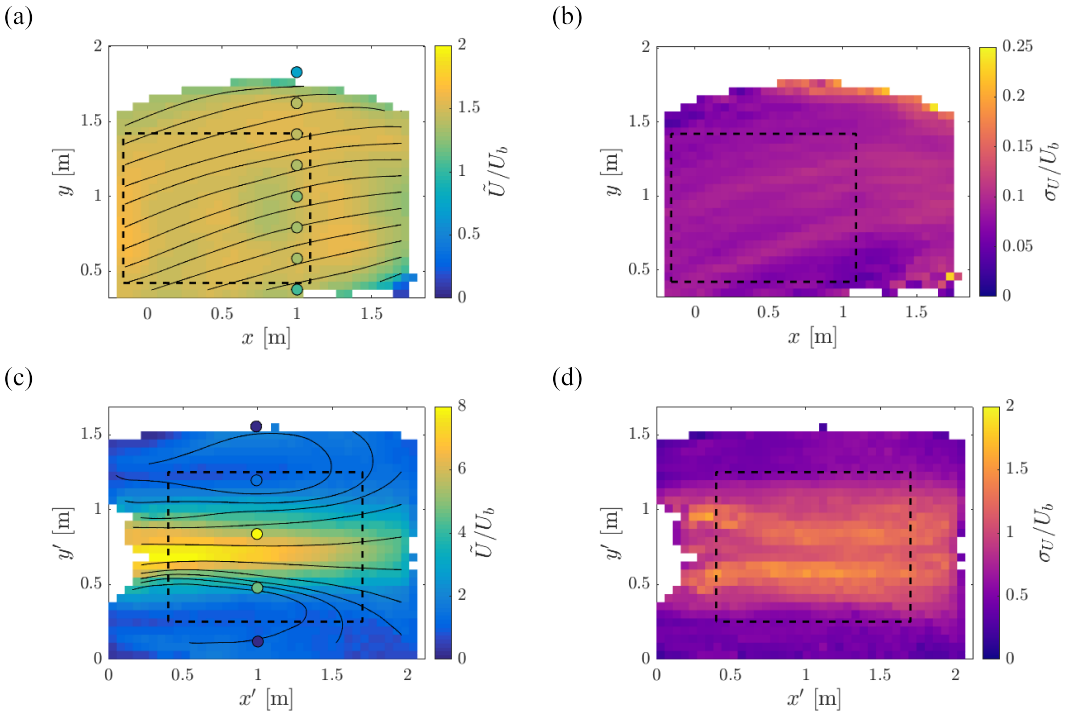

Figure 7. Eulerian mean velocity (a-c) and RMS velocity fluctuation (b-d) fields of the tracers for Q_1, normalized by the bulk velocity; meander (a-b) and pool (c-d). The black lines indicate streamlines and the dashed boxes indicate the sub-regions where Lagrangian quantities are evaluated. The coloured circles (a-c) correspond to the near-surface ADV measurements of $\overline{u}_x$ along the cross-section $x = x' = 1$.

7. Also displayed are the near-surface (2 cm depth) ADV measurements. These reasonably agree with the Eulerian fields obtained by PTV, except for the regions near the shallow banks. As anticipated, the meander displays a remarkably homogeneous surface flow. In particular, we define a 1.25 × 1 m sub-region in it (highlighted in the figure) where $\tilde{U}$ and σ_U remain within ±2.5 % and 9.3 % of their respective spatial mean and the streamlines are relatively straight. In this sub-region we investigate unbiased single-point and two-point flow statistics, characterizing the spatio-temporal flow scales, using the framework of homogeneous turbulence (presented in the next section), and examine the Lagrangian particle transport. On the other hand, the jet-like flow structure in the pool is clearly visible with two shear layers associated with large velocity fluctuations and flanked by recirculation zones (Figure 7c). Because of the significant spatial inhomogeneity, the scales of the free surface turbulence in the pool are not carried out, as this would require spatial averaging and the evaluation of velocity fluctuations around a local mean. The Lagrangian particle transport in this ROI is quantified in a 1.1 × 1 m sub-region. For both ROIs, the choice of the sub-region avoids statistics being strongly influenced by the proximity of the banks and reduces potential bias from short trajectories as the particles exit the FOV.

3.3 Free Surface Turbulence in the Meander

For statistical analysis of the free surface turbulence, we are particularly interested in the instantaneous velocity fluctuations. For this purpose, the particle velocity fluctuations $u_i'(t)$ are calculated by subtracting from the measured velocity $\vec{u}(t)$ the global mean $\langle\vec{u}\rangle$, hence $u_i(t) = \langle u_i\rangle + u_i'(t)$, known as Reynolds decomposition. The mean flow velocity vector

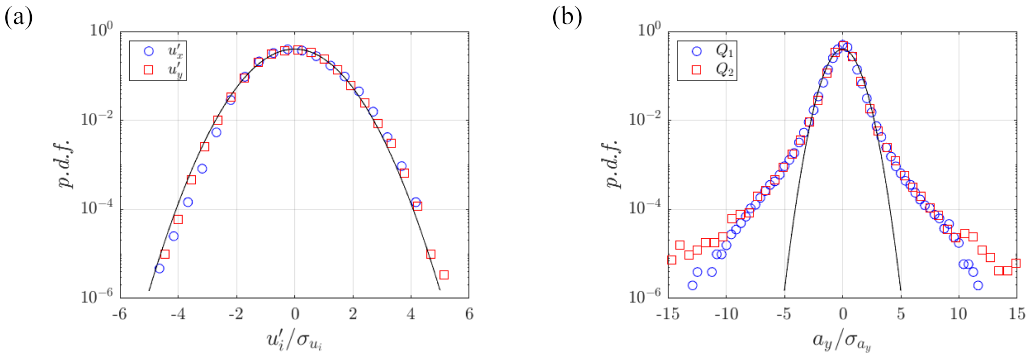

Figure 8. (a) Streamwise and spanwise velocity fluctuation *p.d.f.* of the spheres in the meander for Q_2. (b) Spanwise acceleration *p.d.f.* for both flow rates. The distributions are normalized by their respective RMS quantities. The continuous line represents the normalized Gaussian distribution.

$\langle\vec{u}\rangle$ is evaluated by ensemble averaging the free surface velocity vector $\vec{u}(t)$ of the spheres obtained by PTV and the subscript i specifies the 2D velocity component. Figure 8 displays the *p.d.f.* of the streamwise (u'_x) and spanwise (u'_y) velocity fluctuations for Q_2, as well as the *p.d.f.* of the spanwise accelerations (a_y) for both flow rates; all quantities are normalized by their respective RMS quantities. Both components of the velocity fluctuations are normally distributed. Conversely, the acceleration *p.d.f.* possesses long exponential tails, indicating strong intermittency (i.e., a relatively large probability of extreme events occurring, especially for the higher Reynolds number). This behaviour of Lagrangian accelerations has been well documented in 3D turbulence (Voth et al., 2002; Mordant et al., 2004; Toschi & Bodenschatz, 2009). While the kurtosis of the velocity fluctuations approximately equals the Gaussian value of 3, the acceleration kurtosis is 8.1 and 15.9 for Q_1 and Q_2, respectively. These levels of intermittency are typical of fully developed 3D turbulence (Voth et al., 2002; Ishihara et al., 2007).

To characterize how the turbulent energy is distributed across the scales of the flow, we consider the Eulerian second-order velocity structure function $S_2^E(\vec{r})$ (Kolmogorov, 1941; Pope, 2000). This is defined as the second moment of the velocity difference $\delta^E\vec{u}(\vec{r}) = \vec{u}(\vec{x},t) - \vec{u}(\vec{x}+\vec{r},t)$, where $\vec{u}(\vec{x},t)$ and $\vec{u}(\vec{x}+\vec{r},t)$ are the velocities of two particles separated by a distance $\vec{r}$ at a given time t

$$S_2^E(\vec{r}) = \langle \delta^E\vec{u}(\vec{r})^2 \rangle \tag{1}$$

Leveraging spatial homogeneity and isotropy, we ensemble-average over all particle pairs at a distance $r = \sqrt{\vec{r}\cdot\vec{r}}$. The ensemble-averaging requires binning the data over ranges of separation $r \pm \Delta r$, where we take $\Delta r = 1$ mm as a trade-off between resolution in scale-space and statistical convergence. Here we focus on the longitudinal structure function, in which the velocity component parallel to the separation vector $\vec{r}$ is considered. Figure 9a shows that this exhibits an approximate $r^{2/3}$ scaling over separations from about 3 cm to 10 cm which is equivalent to the $k^{-5/3}$ scaling of the velocity spectra (Figure 6). This suggests the validity of the Kolmogorov (1941) ansatz in the inertial sub-range, hence

$$S_2^E(r) = C_2(\epsilon r)^{2/3} \tag{2}$$

where ϵ is the dissipation rate of the turbulent kinetic energy, and C_2 is a constant. Furthermore, Flores et al. (2017) report that even though the mechanism underlying the $k^{-5/3}$

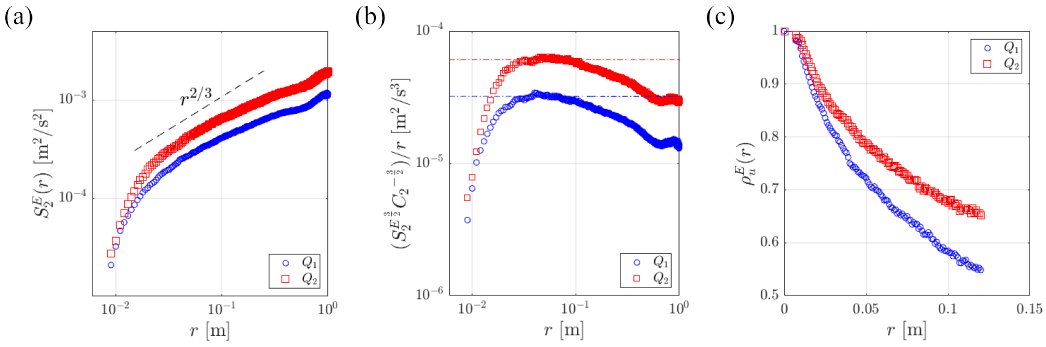

Figure 9. (a) Eulerian longitudinal second-order structure function, (b) compensated structure function and (c) Eulerian velocity autocorrelation function of the tracers for both flow rates. The dashed line in (a) corresponds to $r^{2/3}$ scaling. The dashed-dotted horizontal lines in (b) show the plateau of the compensated structure function which corresponds to the turbulent dissipation rate.

spectral slope at the near-surface may differ from the 3D turbulence dynamics in the bulk, the proportionality constants are roughly the same. Therefore, we assume $C_2 = 2.1$ as in 3D turbulence (Pope, 2000; Saddoughi & Veeravalli, 1994) and use Equation 2 to estimate ϵ from the plateau of the compensated structure functions in Figure 9b. We then estimate the dissipative scales of the free surface turbulence: the Kolmogorov length and time scale, respectively

$$\eta = \left(\frac{\nu^3}{\epsilon}\right)^{1/4} \tag{3}$$

$$\tau_\eta = \left(\frac{\nu}{\epsilon}\right)^{1/2} \tag{4}$$

To determine the integral scales of the free surface turbulence, we make use of the Eulerian velocity autocorrelation function, which for homogeneous turbulence can be easily derived from the second-order structure function

$$\rho_i^E(r) = \frac{\langle u_i'(\vec{x},t)u_i'(\vec{x}+\vec{r},t)\rangle}{\sigma_i^2} = 1 - \frac{S_2^E(r)}{2\sigma_i^2} \tag{5}$$

where σ_i^2 is the variance of u_i'. The obtained velocity correlation exhibits an approximately exponential decay (Figure 9c), and the integral length scale L is evaluated by least-square fitting to it a function $Ae^{-r/L}$ where A is a constant of order unity. The estimates for the dissipative and integral scales, summarized in Table 3, support the notion that the $r^{2/3}$ scaling of the structure function applies over an inertial sub-range $\eta \ll r \ll L$. Additionally, an alternative estimate of the dissipation rate can be obtained from the classic scaling (Tennekes & Lumley, 1972)

$$\epsilon \approx C\frac{\sigma_u^3}{L} \tag{6}$$

Taking the typical proportionality constant $C = 0.5$ as for 3D turbulence in the high-Reynolds number limit (Burattini et al., 2005; Carter et al., 2016), we obtain dissipation estimates consistent with those found from the second-order structure function.

Table 3. Main physical quantities characterizing the free surface turbulence for both flow rates in the Meander: RMS of the velocity fluctuations σ_u, dissipation rate of turbulent kinetic energy ϵ, integral length scales L, integral time scale T_L, Kolmogorov length scale η, and Kolmogorov time scale τ_η.

Meander	σ_u [$\mathrm{m\,s^{-1}}$]	ϵ [$\mathrm{m^2\,s^{-3}}$]	L [m]	T_L [s]	η [mm]	τ_η [s]
$Q_1 = 32.1\,\mathrm{L\,s^{-1}}$	0.022	$3.2 \cdot 10^{-5}$	0.175	1.02	0.4	0.18
$Q_2 = 53.7\,\mathrm{L\,s^{-1}}$	0.032	$6.1 \cdot 10^{-5}$	0.243	1.01	0.4	0.13

3.4 Effect of Particle Shape and Size in the Meander

In this section, we compare the motion of the larger particles (discs and rods) against the spheres. We start by considering the meander where the flow homogeneity allows for a comprehensive statistical description of the transport.

The Eulerian velocity fields of all particle types are found to be quantitatively similar. This is evident from Figure 10a-b, where the velocities of the larger particles are normalized by those of the spheres. For both considered flow rates, the RMS difference between the three particle types and the near-surface ADV measurements is less than 2 % of $\tilde{U}$ and less than 17 % of σ_U. Also displayed are the particle velocity and acceleration *p.d.f.* for selected components and flow rates (Figure 10c-d). To highlight the difference between the different particle types, the Kolmogorov velocity scale $u_\eta = \eta/\tau_\eta$ and acceleration scale $a_\eta = u_\eta/\tau_\eta$ are used for normalization. The velocity fluctuations are similar between all particle types, closely approximating a Gaussian distribution (Figure 10c). Contrarily, the acceleration intermittency shown by the spheres is significantly reduced for the larger particles (Figure 10d). Moreover, at Q_1, the RMS acceleration of the discs and rods is 9 % and 21 % lower than that of the tracers, respectively, while at Q_2 the reduction becomes 8 % and 20 %, respectively.

To characterize the spreading rate of the floating particles, we consider their Lagrangian motion characterized by single-particle dispersion; examining how far, on average, a single particle migrates from its origin over time. Leveraging the homogeneity of the flow in the meander and following the classic framework of Taylor (1921), the single-particle diffusivity can be derived from the Lagrangian velocity autocorrelation

$$\rho_u^L(\tau) = \left\langle \frac{\sum \vec{u}'(t) \cdot \vec{u}'(t+\tau)}{\sum \vec{u}'(t)^2} \right\rangle \tag{7}$$

Here, the summation extends to all values of τ along each trajectory (i.e., the autocorrelation is first calculated along each trajectory and normalized by its velocity variance, before ensemble-averaging over all trajectories). This ensures that each trajectory has the same weight when contributing to the global autocorrelation coefficient (Guala et al., 2007). Additionally, we only consider trajectories whose duration is longer than the time delay τ (Mordant et al., 2004). Figure 11a-b display the Lagrangian velocity autocorrelation of each particle type for both considered flow rates, showing that the motion of the discs and rods is more time-correlated than that of the spheres. This is consistent with the trend reported by numerical simulations of inertial particles (Squires & Eaton, 1991; Jung et al., 2008) and laboratory observations of finite-size particles (Machicoane & Volk, 2016) in 3D turbulence.

The diffusivity K is obtained by integrating the decaying Lagrangian velocity autocorrelation (Taylor, 1921)

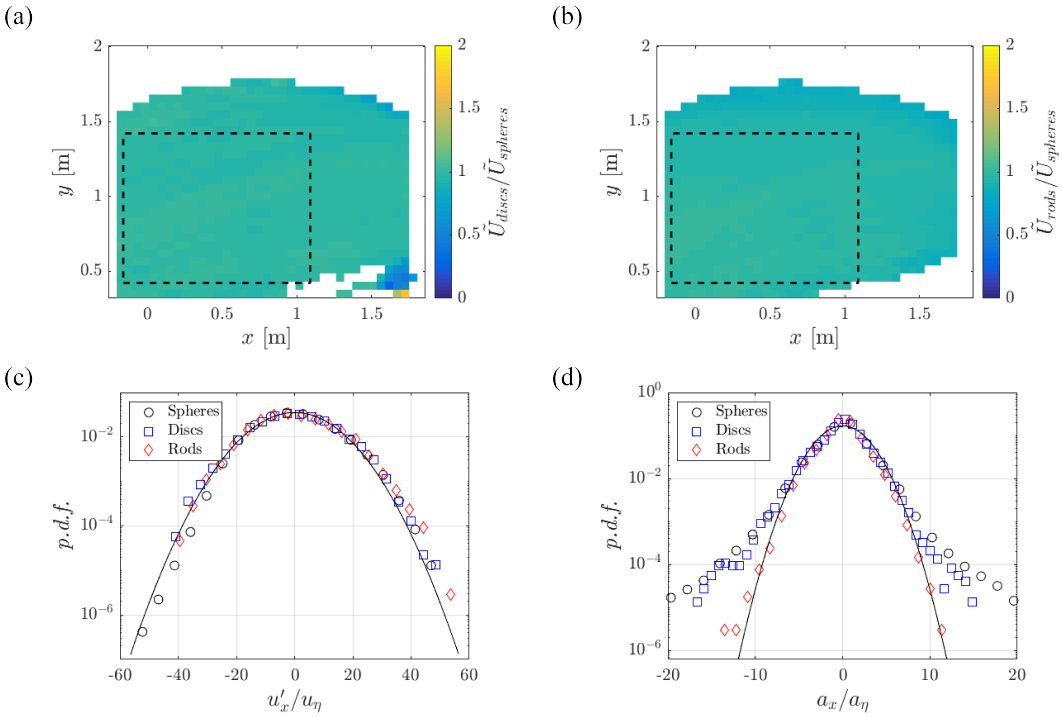

Figure 10. Eulerian mean velocity fields of the discs (a) and rods (b) for Q_1. (c) Streamwise velocity fluctuation *p.d.f.* of the different particle types in the meander for Q_2. (d) Streamwise acceleration *p.d.f.* of the different particle types in the same location for Q_1. The distributions are normalized by Kolmogorov scaling. The continuous line represents the normalized Gaussian distribution.

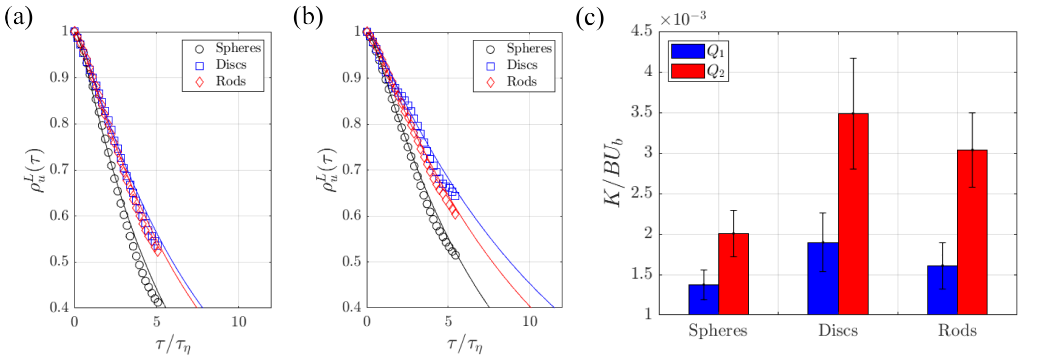

Figure 11. Lagrangian velocity autocorrelation function of each particle type for Q_1 (a) and Q_2 (b). The solid lines are the autocorrelation functions computed using Equation 9 which are integrated to obtain diffusion coefficients. (c) Normalized diffusivity of the different particle types for both flow rates. The error bars represent the standard deviation of the diffusion coefficients from separate runs.

$$K = \sigma_u^2 \int_0^\infty \rho_u^L(\tau) d\tau \tag{8}$$

As the extreme of integration grows, the autocorrelation is expected to decay to negligibly small values and correspondingly the diffusivity will asymptote to a value independent of time. Due to the finite length of the recorded trajectories, we extrapolate the autocorrelation using the stochastic model proposed by Sawford (1991)

$$\rho_u^L(\tau) = \frac{T_L e^{-\tau/T_L} - T_2 e^{-\tau/T_2}}{T_L - T_2} \tag{9}$$

Here, two time scales are required: the integral time scale of the turbulence T_L, and a characteristic time scale related to the dissipation T_2. The former is defined as the characteristic decay time of the Lagrangian velocity autocorrelation function of the spheres and is estimated by least-square fitting $\rho_u^L(\tau)$ to an exponential function of the form e^{-t/T_L}, and reported in Table 3. The value of T_2 is estimated by fitting the experimental curve to Equation 9 and found to be approximately $0.3\tau_\eta$; this is the same order of magnitude as in 3D turbulence studies (Voth et al., 2002; Mordant et al., 2004). The diffusivity is then determined by the long-time asymptote of K using Equations 8 and 9. For the spheres we obtain normalized diffusivities $K/u_\tau d_p \approx 0.5$ for both flow rates, where we estimate the friction velocity u_τ from its relationship with the dissipation rate, $\epsilon = {u_\tau}^3/d_p$ (assumed to be mainly driven by bed friction (Raymond et al., 2012)). This falls well in the range $K/u_\tau d_p = 0.3$ to 0.9 reported for meandering channels (Fischer et al., 1979; Rutherford, 1994). The diffusivity is plotted in Figure 11c for the different particle types and for both considered flow rates. One clearly sees an increase in K with increasing flow rate, hence with Reynolds number. Most importantly, the larger particles exhibit larger diffusivity than the spheres, with the discs spreading faster than the rods. We remark that the extrapolation using Sawford (1991) model adds quantitative uncertainty to the estimated value of K. Therefore below, we report measures of the Lagrangian transport that are not affected by such extrapolation.

Next, we consider the mean square displacement (MSD) of recorded PTV trajectories due to turbulent fluctuations

$$\langle X(t)^2 \rangle = \langle \| \vec{x}_p(t) - \vec{x}_p(t_0) - \langle \vec{u} \rangle \Delta t \|^2 \rangle \tag{10}$$

where $\vec{x}_p(t)$ is the particle position at time t and $\vec{x}_p(t_0)$ is the reference position at the temporal origin of the trajectory t_0. The advective displacement $\langle \vec{u} \rangle \Delta t$, due to the mean flow during the time interval $\Delta t = t - t_0$, is subtracted to isolate the contribution of the turbulent fluctuations. Leveraging spatial homogeneity, the advective flow is taken to be a uniform motion, which avoids the ambiguities associated with subtracting different advective displacements at different points along the same trajectory. The MSD of each particle type for both flow rates is plotted in Figure 12a-b and confirms that the discs spread faster than the rods, which spread faster than the spheres. Calculating the diffusivity from a least-square fit to the linear part of the MSD returns a value of diffusivity in agreement with those reported above. Although not shown, we also note that the MSD can alternatively be computed by integrating the autocorrelation twice (Taylor, 1921; Pope, 2000)

$$\langle X(t)^2 \rangle = 2\sigma_u^2 \int_0^t \int_0^{t'} \rho_u^L(\tau) d\tau dt' \tag{11}$$

where t' is a second integration variable. This yields analogous trends when compared to Equation 10.

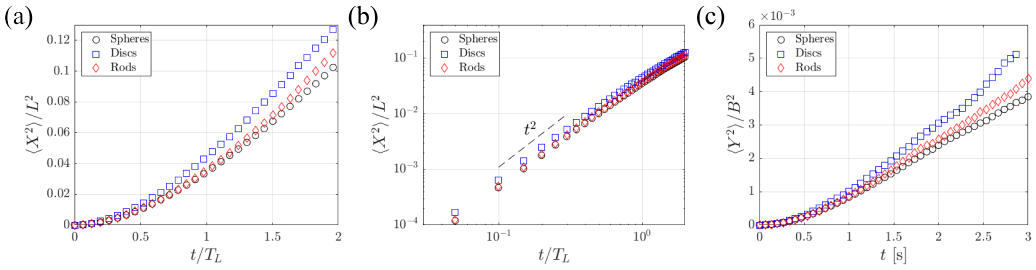

Figure 12. Normalized MSD due to turbulent velocity fluctuations of each particle type in the meander for Q_1 (a) and Q_2 (b). (c) Spanwise MSD of the different particles in the pool for Q_1.

3.5 Effect of Particle Shape and Size in the Pool

In this section, we verify that the trends observed in the meander also apply to the significantly different flow conditions found in the pool. Also here, the Eulerian fields of $\tilde{U}$ and σ_U for the discs and rods (not shown) are close to those measured for the spheres, shown in Figure 7c-d, with RMS difference between the three particle types and the near-surface ADV measurements less than 12 % for $\tilde{U}$ and less than 16 % for σ_U. Nevertheless, as for the meander, we shall see that the particle shape and size influences the Lagrangian dispersion.

Because the mean velocity in the pool is predominantly aligned with x', we can isolate the turbulent dispersion by considering the lateral displacement (i.e., the MSD of particle trajectories along the spanwise direction y')

$$\langle Y(t)^2\rangle = \langle [y'(t) - y'(t_0)]^2\rangle \tag{12}$$

and is plotted in Figure 12c for Q_1 (Q_2 displaying analogous results). This indicates again that the larger particles spread faster than the spheres, with the discs spreading faster than the rods. An estimate of the lateral diffusion coefficient can be derived from the relation

$$K_{y'} = \frac{1}{2}\frac{d\langle Y(t)^2\rangle}{dt} \tag{13}$$

A linear least-square fit to the data over the range $t > 1.5\,\mathrm{s}$ (where the MSD is approximately linear with time) yields $K_{y'} = 0.002\,\mathrm{m^2\,s^{-1}}$, $0.003\,\mathrm{m^2\,s^{-1}}$ and $0.0025\,\mathrm{m^2\,s^{-1}}$ for the tracers, discs, and rods, respectively.

3.6 Rotational dynamics

The translational and rotational motion of anisotropic particles in turbulence are strongly coupled to each other (Voth & Soldati, 2017). Therefore, we consider the rotational dynamics of the rods, as it can provide insight into the transport behaviour presented in the previous section. We present results for Q_2, with Q_1 showing analogous trends.

We first consider the alignment of the rods defined by the orientation vector $\hat{p}(t)$. Figure 13a shows the *p.d.f.* of $|\hat{p}(t)\cdot\hat{u}(t)|$, where $\hat{u}(t)$ is the unit vector parallel to the particle velocity. For both ROIs, the rods display a preference to align with the direction of motion. Considering the close similarity between the velocity fields of the spheres and those of the rods, this can be interpreted as a preferential alignment with the flow direction.

The intermittent nature of the free surface turbulence, displayed in the acceleration *p.d.f.* in Figure 8b, is also reflected in the distribution of the angular velocity Ω shown in Figure 13b. The kurtosis of these distributions are 5.9 and 8.8 for the meander and the

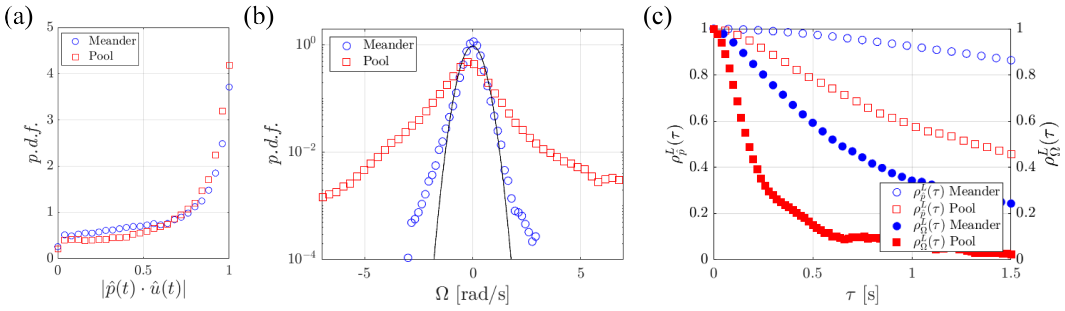

Figure 13. (a) The *p.d.f.* of the absolute value of the cosine of the orientation angle of the rods in both ROIs. (b) The *p.d.f.* of the angular velocities in both ROIs. (c) Lagrangian autocorrelation functions of the rods' orientation and angular velocity in both ROIs.

pool, respectively, indicating a relatively large probability of extreme events with angular velocities of several rad s^{-1}, especially with a higher turbulence intensity of the free surface. Such sudden changes in orientation are expected to alter the Lagrangian transport by the underlying flow.

The curvature of the streamlines in the ROIs is small, but the rods' orientation varies in time due to flow fluctuations. We characterize the time scales associated with the rods' re-orientation by the Lagrangian autocorrelation of the orientation vector $\rho^L_{\hat{p}}(\tau)$, calculated analogously to the velocity autocorrelation function in Equation 10 and shown in Figure 13c. In the meander the particle orientation is remarkably stable, which is consistent with its moderate turbulence intensity: the fluid velocity, with which the rods tend to be aligned, remains mostly oriented in the streamwise direction. The orientation autocorrelation in the pool shows a faster decay with a characteristic time of approximately 1.5 s. Given the jet-like flow structure, a candidate time scale dictating the rod reorientation is provided by the intense shear layers (Figure 7c-d). Indeed, visual observation confirms that the rods' rotation in those regions follows the direction of the mean shear. The associated time scale can be estimated from the jet half-width $d_{1/2} \approx 0.5$ m and the velocity difference across it $\Delta\tilde{U} \approx 0.4\,\mathrm{m\,s^{-1}}$ such that $d_{1/2}/\Delta\tilde{U} \approx 1.25$ s, which approximately agrees with the observed correlation time scale. The fact that the time scale of re-orientation is attributed to the mean shear of the surface flow is consistent with the observation that the rods' orientation is very stable in the meander, where the flow is highly homogeneous and lateral shear is weak.

Figure 13c also shows the autocorrelation of the angular velocity $\rho^L_{\Omega}(\tau)$, which as expected decays significantly faster than $\rho^L_{\hat{p}}(\tau)$. For the meander, the correlation time scale of $\rho^L_{\Omega}(\tau)$ is approximately 1 s, matching the integral time scale of the free surface turbulence T_L. In the pool, the same quantity decays with a characteristic time scale around 0.25 s. While a single value of T_L can hardly be defined in the pool due to spatial inhomogeneity, we note that σ_U is roughly 4 times larger than in the meander. This suggests that, in both ROIs, the correlation time scale of $\rho^L_{\Omega}(\tau)$ is dictated by the energetic eddies that determine the integral scales of the turbulence. Since the rods' length is two orders of magnitude larger than η and a fraction of L, this finding is in line with the view that rods' rotation is controlled by eddies of size comparable to or larger than their length (Parsa & Voth, 2014; Voth & Soldati, 2017).

3.7 Laboratory Results

The analysis of the laboratory measurements is analogous to the outdoor stream study. The trajectory trajectories are first binned into 4 mm × 4 mm interrogation windows to

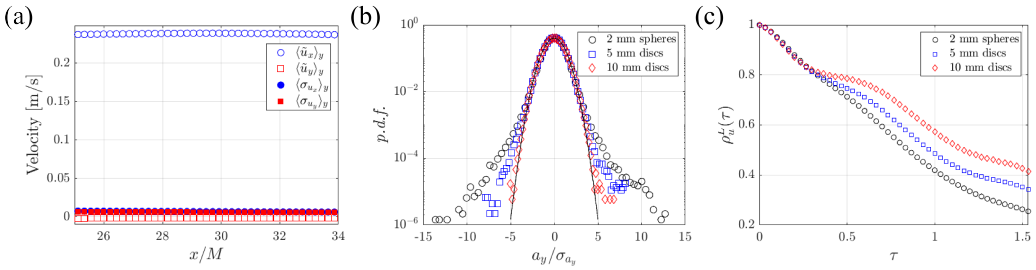

Figure 14. (a) The spanwise average of both components of the mean velocity and RMS fluctuations for the tracers. (b) Spanwise acceleration *p.d.f.* of the different particles normalized by their respective standard deviations. (c) Lagrangian velocity autocorrelation for the different particle types (c).

generate Eulerian mean fields. In this case, as expected, the degree of homogeneity is much higher, and therefore the presented data is obtained from an ROI that coincides with the FOV. A similar analysis to the one presented for the meander indicates that $\epsilon = 2 \cdot 10^{-5}$ $\mathrm{m^2\,s^{-3}}$ on the free surface, for $\eta = 0.5\,\mathrm{mm}$. Figure 14a displays the spanwise average of both components of the mean velocity $\langle \tilde{u}_i \rangle_y$ and RMS fluctuations $\langle \sigma_i \rangle_y$ for the tracers, indicating nearly isotropic turbulence along the free surface. Figure 14b displays the *p.d.f.* of the spanwise acceleration a_y for each particle type normalized by their respective standard deviation. As in the outdoor stream, there is an apparent reduction in intermittency for the larger particles when compared to the tracers, with the larger discs displaying almost Gaussian accelerations. Finally, Figure 14c shows the Lagrangian velocity autocorrelation for the different particle types. Clearly, the motion of the larger particles has a degree of temporal correlation that increases with particle size.

4 Discussion

The PTV measurements of the small spheres, especially in the spatially homogeneous sub-region of the meander, inform us of the nature of the free surface flow in the considered riverine environment. We remark that, for fundamental reasons, free surface turbulence is not expected to be equivalent either to 2D or 3D turbulence: the surface exchanges energy and enstrophy with the flow underneath, hence neither quantity can be regarded as invariant and dimensional scaling arguments do not strictly apply (Cressman et al., 2004). However, the present measurements do indicate a strong similarity with the phenomenology of 3D turbulence. In particular, the behaviour of the second-order structure function is consistent with Kolmogorov (1941) scaling in the inertial sub-range. While a similar scaling is also expected in the inverse-cascade range of 2D turbulence (Kraichnan, 1967), the latter framework is inconsistent with the observed intermittency of the acceleration (Boffetta & Ecke, 2012). The close agreement between the dissipation estimates from Equations 2 and 9 further supports the applicability of a 3D turbulence framework. The similarity between 3D and free surface turbulence is possibly due to the surface carrying the prominent imprint of sub-surface vortices connected to it. These evolve by diffusion and stretching, as vortex tilting is annihilated at the surface (Shen et al., 1999; C. Zhang et al., 1999; Shen & Yue, 2001). In other words, unlike in 2D turbulence, the free surface boundary condition affects but does not suppress vortex stretching, which is essential to the energy cascade in 3D turbulence (Davidson, 2015; Carbone & Bragg, 2020; Johnson, 2020).

Our results are specific to a particular riverine flow configuration, therefore further studies are needed to assess the generality of the observations, especially as a function of the water depth, which is known to influence the turbulence dynamics (Nezu et al., 1994). Additionally, water depth influences the respective role of water-column turbulence and

bed friction in setting the dissipation rate at the surface (Raymond et al., 2012; Ulseth et al., 2019). Moreover, vortex stretching is hindered in shallow flows, which can trigger the emergence of features peculiar to 2D turbulence (Uijttewaal & Booij, 2000; Stocchino et al., 2011).

Our main finding is that, in both investigated ROIs, larger floating particles disperse faster than smaller tracer-like particles. This result can be interpreted based on our understanding of the behaviour of inertial particles in turbulence. We remind that the term "inertial" indicates objects too heavy and/or too large to faithfully follow the fluid flow (Brandt & Coletti, 2022). Indeed, both discs and rods display weaker and less intermittent accelerations than the spheres. This behaviour is well known from the investigation of 3D turbulence laden with inertial particles and is attributed to two concurring mechanisms: preferential sampling of high-strain/low-vorticity regions, prevalent for small St, and inertial filtering of the small-scale/high-frequency fluctuations, prevalent for $\mathrm{St} \gg 1$ (Bec et al., 2006; Toschi & Bodenschatz, 2009). Here we have estimated $\mathrm{St} = \mathcal{O}(10)$ for the cm-sized particles. This supports inertial filtering as the likely cause of the observed behaviour. These relatively large particles respond to a spatial average of the fluid velocity, making them less sensitive to the smaller and faster-decaying eddies. This is consistent with the increasingly time-correlated motion of the larger particles. The trends found in the outdoor stream have also been confirmed by a dedicated laboratory study of similar regimes, indicating that the conclusions possess a degree of generality. The slower decay of the velocity autocorrelation is consistent with the simulations of Shin and Koch (2005) for rods in 3D turbulence, who found the correlation time scale T_L to increase with the rods' length. However, in such a study, the RMS velocity fluctuations of the rods σ_u were found to decrease with their length, and the diffusivity $K = {\sigma_u}^2 T_L$ ultimately decreased. We remark that our estimate of St is consistent with previous studies on inertial particles in turbulence. In particular, based on the direct numerical simulations of Jung et al. (2008), particles with $\mathrm{St} = \mathcal{O}(10)$ in homogeneous turbulence have a Lagrangian integral time scale ~ 2.0 times larger than the one of tracers (see their Figure 6a); this is consistent with our observations for the discs. In their study, however, the inertial particles also showed a significant reduction in fluctuating velocity, hence the increase of the inertial particle diffusivity was milder. In the present case, the RMS velocity fluctuations of the particles are not significantly affected by their size and shape, and thus the diffusivity follows the same trend as T_L. The fact that the particles are relatively large (as opposed to material points, as in Jung et al. (2008)) may be the cause of the difference. Also, their simulations spanned a limited range of scales, $L/\eta < 30$. In such a situation, particles with $\mathrm{St} = \mathcal{O}(10)$ based on the Kolmogorov time scale have a response time comparable to the integral time scale of the turbulence, which may result in the significant reduction of the fluctuating energy of the particles.

Despite the rods' length being almost twice the discs' diameter, the latter disperse faster than the former. This may be due to the discs possessing a larger wetted area, thus more effective filtering of the small-scale fluctuations. However, the object shape is also likely to have a profound influence on the Lagrangian transport. The characteristic time scale of Ω and its intermittent nature indicate that the instantaneous orientation of the rods is affected by a range of turbulent scales. These may contribute to decorrelating their translational motion, which for anisotropic particles is strongly coupled with the rotational motion (Voth & Soldati, 2017). Moreover, the rods' tendency to align with the flow direction suggests that the large scales of the turbulence (at least those larger than the rods' length) are not isotropic and likely populated by streamwise-oriented structures. Indeed, already early studies of open channel flows highlighted the connection between near-wall bursts in the bottom-wall boundary layer and the coherent motions that transfer mass to and from the free surface (Nakagawa & Nezu, 1981; Rashidi & Banerjee, 1988). The complex bed topography of a natural channel is likely to enhance this connection by generating energetic eddies that can travel up to the surface, as indicated by the fact that bed roughness in shallow streams strongly correlates with gas transfer velocity (Ulseth et al., 2019).

Besides shape and size, other properties of floating particles may be influential towards their free surface transport; in particular, bulk density and surface characteristics. Particles of higher density and mass may be more effective in filtering small-scale turbulent fluctuations, which could further enhance their diffusivity. However, depending on the size, this effect could be counteracted by a lack of responsiveness to some of the energetic scales responsible for dispersion. Moreover, density and surface characteristics, in particular hydrophobicity, will affect the balance between surface tension and gravity, determining the submerged fraction of the floating object (Koh et al., 2009; Ji et al., 2018). In turn, submergence will determine the amount of windage, i.e., the drag exerted by the airflow on objects partly protruding out of the water (Zambianchi et al., 2014; Beron-Vera et al., 2019). Finally, while we have limited our study to sparse objects that do not significantly interact with each other, compressibility of the free surface flow is known to produce intense clustering that can bring floaters into close contact (Cressman et al., 2004; Lovecchio et al., 2013). Again, the material properties of the particles are then expected to affect the short-range interactions and possibly lead to aggregation (Vella & Mahadevan, 2005). The impact of such particle properties, which is outside the scope of the present work, clearly warrants further systematic investigations using different particle materials.

The observed influence of the particles' properties on dispersion, once confirmed for a wider range of particle types and flow conditions, may have profound implications for the transport of floating particles; in particular, the transport of meso- and macroplastics in small streams and turbulent waters in general. The diffusivity, which we find to roughly double from mm-sized to cm-sized objects, is a crucial quantity to incorporate the effect of unresolved spatio-temporal scales in Lagrangian transport models for rivers, lakes, and the oceans (Liu et al., 2011; Park et al., 2017; van Sebille et al., 2018; Daily & Hoffman, 2020; McDonald & Nelson, 2021). Our results indicate that such a parameter varies significantly not only with the flow conditions but also with the particle properties. Parameterizations that also include the latter appear necessary to obtain accurate predictions from such models.

5 Conclusion

Motivated by the need of understanding the transport of plastic litter in river flows, we have used time-resolved PTV to characterize the motion of particles of different shape and size floating on the surface of a field-scale meandering stream. We have considered two locations with different turbulence levels, in which the role of surface waves on the transport is deemed negligible. We have measured the position, velocity, and acceleration along the trajectories of thousands of millimetre-sized spherical pellets and centimetre-sized discs and rods, as well as the orientation and rotation of the latter, and evaluated the spatio-temporal scales associated with such quantities. At the meander, the homogeneity of the flow properties allows us to identify both dissipative and integral scales of the free surface turbulence, providing essential terms of comparison for the size of the particles and the scales of their motion. The spheres are small enough to capture most if not all scales of the free surface motion and are regarded as flow tracers; while the length of the rods and the diameter of the discs are $\mathcal{O}(100)$ times larger than the dissipative scales and several times smaller than the integral scales of the turbulence. The analysis of the particles' motion leads to the following observations:

I. All considered particles display almost indistinguishable mean velocities and RMS velocity fluctuations. These are determined by the largest scales of the surface flow, to which the particles respond faithfully.
II. While the velocity fluctuations follow normal distributions unaffected by the particle shape and size, the accelerations show a sizeable degree of intermittency which decreases for larger particles. This is attributed to the finite size of the particles, filtering out the smallest scales of the turbulence associated with the most intense gradients.

III. Consequently, the larger particles spread more rapidly on the turbulent free surface, with diffusivity coefficients roughly doubling for centimetre-sized particles as compared to millimetre-sized tracers. This is due to the motion of the larger particles being more time-correlated, which in turn is rooted in their impaired response to the small-scale turbulent fluctuations.
IV. The rods tend to align with the flow direction, but their instantaneous orientation is influenced by a range of scales: they re-orient following the mean shear, rotate according to the turnover time of the energetic eddies, and exhibit intermittency in their angular velocities. This leads to less time-correlated motions and slower dispersion than the discs, despite the rods' length being larger than the discs' diameter.

Overall, the behaviour of the free surface turbulence and the motion of particles floating on it appears to be consistent with the phenomenology of inertial finite-sized particles in 3D turbulence. This similarity, to be confirmed in a wider range of flow conditions and particle types, may allow leveraging of established results and recent advances in the field of particle-laden turbulence (Balachandar & Eaton, 2010; Brandt & Coletti, 2022), furthering the predictive understanding of the transport of floating plastics in natural waters. We observe that the shape and size of floating particles in turbulent streaming waters only affects the higher-order statistics (which in turn influences the Lagrangian transport), while the mean velocity and RMS fluctuations are not measurably affected. This may be valuable for modelling the transport of non-spherical floating particles in rivers.

Future studies shall expand the present work in several directions. Our experiments have been carried out in a relatively small stream; studies in larger and deeper rivers, in which the dissipation mechanisms in the water column are inherently different (Moog & Jirka, 1999), are needed to expand and generalize the results. In such cases, particle imaging may require the use of uncrewed aerial vehicles, which have been successfully utilized to characterize natural flows (Blois et al., 2016; Liu et al., 2021). Given the variety of debris types found in water streams, the range of particle properties should be expanded beyond shape, size, and density: deformability and brittleness have recently been investigated in laboratory studies and are especially relevant to plastic pollution (Brouzet et al., 2014, 2021). Finally, high-Froude streams and/or streams under the action of wind where breaking and non-breaking waves occur may play a major role in the transport of floating particles. The recent laboratory experiments of Lenain et al. (2019), confirming computational results by Deike et al. (2017), found that breaking waves induce much stronger transport of cm-sized spherical particles compared to Stokes drift. Moreover, Ruth et al. (2022) showed that bubbles entrained during wave-breaking events travel downstream faster than the Stokes drift associated to buoyant particles in non-breaking waves. Overall, studies investigating the effect of particle properties in wave-breaking conditions are warranted.

Open Research

Data - Pre-processed background-subtracted images for the different regions of interest and flow rates and particles are available at `https://doi.org/10.3929/ethz-b-000572787`.

Data - Smoothed particle trajectories for the different regions of interest and flow rates and particles are available at `https://doi.org/10.3929/ethz-b-000573259`.

Software - Analysis and figures were done with MATLAB version R2020a, available under the MATLAB license at `https://mathworks.com/`.

Acknowledgments

This work was supported by the Environmental and Natural Resources Trust Fund (ENTRF) whose purpose is to provide a long-term, consistent, and stable source of funding for activities that protect, conserve, preserve and enhance Minnesota's air, water, land, fish,

wildlife and other natural resources for the benefit of current citizens and future generations. The authors would like to thank Eleanor Arpin and SAFL technical staff for their assistance as well as the Legislative-Citizen Commission on Minnesota Resources (LCCMR) for their funding recommendation to the Minnesota Legislature.

References

Adrian, R. J., & Westerweel, J. (2011). *Particle image velocimetry* (No. 30). Cambridge University Press.

Baker, L. J., & Coletti, F. (2019). Experimental study of negatively buoyant finite-size particles in a turbulent boundary layer up to dense regimes. *Journal of Fluid Mechanics*, *866*, 598–629.

Baker, L. J., & Coletti, F. (2021). Particle–fluid–wall interaction of inertial spherical particles in a turbulent boundary layer. *Journal of Fluid Mechanics*, *908*.

Baker, L. J., & Coletti, F. (2022). Experimental investigation of inertial fibres and disks in a turbulent boundary layer. *Journal of Fluid Mechanics*, *943*.

Balachandar, S., & Eaton, J. K. (2010). Turbulent dispersed multiphase flow. *Annual Review of Fluid Mechanics*, *42*, 111–133.

Ballent, A., Purser, A., de Jesus Mendes, P., Pando, S., & Thomsen, L. (2012). Physical transport properties of marine microplastic pollution. *Biogeosciences Discussions*, *9*(12).

Bec, J., Biferale, L., Boffetta, G., Celani, A., Cencini, M., Lanotte, A., ... Toschi, F. (2006). Acceleration statistics of heavy particles in turbulence. *Journal of Fluid Mechanics*, *550*, 349–358.

Berk, T., & Coletti, F. (2021). Dynamics of small heavy particles in homogeneous turbulence: a lagrangian experimental study. *Journal of Fluid Mechanics*, *917*.

Beron-Vera, F. J., Olascoaga, M. J., & Miron, P. (2019). Building a maxey–riley framework for surface ocean inertial particle dynamics. *Physics of Fluids*, *31*(9), 096602.

Blois, G., Best, J., Christensen, K., Cichella, V., Donahue, A., Hovakimyan, N., ... Pakrasi, I. (2016). Assessing the use of uav to quantify flow processes in rivers. In *River flow.*

Boffetta, G., & Ecke, R. E. (2012). Two-dimensional turbulence. *Annual Review of Fluid Mechanics*, *44*(1), 427–451.

Brandt, L., & Coletti, F. (2022). Particle-laden turbulence: progress and perspectives. *Annual Review of Fluid Mechanics*, *54*, 159–189.

Brocchini, M., & Peregrine, D. (2001). The dynamics of strong turbulence at free surfaces. part 1. description. *Journal of Fluid Mechanics*, *449*, 225–254.

Brouzet, C., Guiné, R., Dalbe, M.-J., Favier, B., Vandenberghe, N., Villermaux, E., & Verhille, G. (2021). Laboratory model for plastic fragmentation in the turbulent ocean. *Physical Review Fluids*, *6*(2), 024601.

Brouzet, C., Verhille, G., & Le Gal, P. (2014). Flexible fiber in a turbulent flow: A macroscopic polymer. *Physical Review Letters*, *112*(7), 074501.

Burattini, P., Lavoie, P., & Antonia, R. A. (2005). On the normalized turbulent energy dissipation rate. *Physics of Fluids*, *17*(9), 098103.

Carbone, M., & Bragg, A. D. (2020). Is vortex stretching the main cause of the turbulent energy cascade? *Journal of Fluid Mechanics*, *883*.

Carter, D., Petersen, A., Amili, O., & Coletti, F. (2016). Generating and controlling homogeneous air turbulence using random jet arrays. *Experiments in Fluids*, *57*(12), 1–15.

Chickadel, C. C., Talke, S. A., Horner-Devine, A. R., & Jessup, A. T. (2011). Infrared-based measurements of velocity, turbulent kinetic energy, and dissipation at the water surface in a tidal river. *IEEE Geoscience and Remote Sensing Letters*, *8*(5), 849–853.

Cressman, J. R., Davoudi, J., Goldburg, W. I., & Schumacher, J. (2004). Eulerian and lagrangian studies in surface flow turbulence. *New Journal of Physics*, *6*(1), 53.

Daily, J., & Hoffman, M. J. (2020). Modeling the three-dimensional transport and distribution of multiple microplastic polymer types in lake erie. *Marine Pollution Bulletin*,

154, 111024.

Davidson, P. A. (2015). *Turbulence: an introduction for scientists and engineers*. Oxford university press.

Deike, L., Pizzo, N., & Melville, W. K. (2017). Lagrangian transport by breaking surface waves. *Journal of Fluid Mechanics*, *829*, 364–391.

De Leo, A., & Stocchino, A. (2022). Dispersion of heavy particles under sea waves. *Physics of Fluids*, *34*(1), 013305.

Del Grosso, N. F., Cappelletti, L. M., Sujovolsky, N. E., Mininni, P. D., & Cobelli, P. J. (2019). Statistics of single and multiple floaters in experiments of surface wave turbulence. *Physical Review Fluids*, *4*(7), 074805.

DiBenedetto, M. H. (2020). Non-breaking wave effects on buoyant particle distributions. *Frontiers in Marine Science*, *7*, 148.

DiBenedetto, M. H., Koseff, J. R., & Ouellette, N. T. (2019). Orientation dynamics of nonspherical particles under surface gravity waves. *Physical Review Fluids*, *4*(3), 034301.

DiBenedetto, M. H., Ouellette, N. T., & Koseff, J. R. (2018). Transport of anisotropic particles under waves. *Journal of Fluid Mechanics*, *837*, 320–340.

Eriksen, M., Mason, S., Wilson, S., Box, C., Zellers, A., Edwards, W., ... Amato, S. (2013). Microplastic pollution in the surface waters of the laurentian great lakes. *Marine Pollution Bulletin*, *77*(1-2), 177–182.

Fiabane, L., Zimmermann, R., Volk, R., Pinton, J.-F., & Bourgoin, M. (2012). Clustering of finite-size particles in turbulence. *Physical Review E*, *86*(3), 035301.

Fischer, H. B., List, J. E., Koh, C. R., Imberger, J., & Brooks, N. H. (1979). *Mixing in inland and coastal waters*. Academic press.

Flores, O., Riley, J. J., & Horner-Devine, A. R. (2017). On the dynamics of turbulence near a free surface. *Journal of Fluid Mechanics*, *821*, 248–265.

Geyer, R., Jambeck, J. R., & Law, K. L. (2017). Production, use, and fate of all plastics ever made. *Science Advances*, *3*(7), e1700782.

Gomit, G., Chatellier, L., & David, L. (2022). Free-surface flow measurements by non-intrusive methods: a survey. *Experiments in Fluids*, *63*(6), 1–25.

Guala, M., Liberzon, A., Tsinober, A., & Kinzelbach, W. (2007). An experimental investigation on lagrangian correlations of small-scale turbulence at low reynolds number. *Journal of Fluid Mechanics*, *574*, 405–427.

Hearst, R. J., & Lavoie, P. (2014). Decay of turbulence generated by a square-fractal-element grid. *Journal of Fluid Mechanics*, *741*, 567–584.

Helinski, O. K., Poor, C. J., & Wolfand, J. M. (2021). Ridding our rivers of plastic: A framework for plastic pollution capture device selection. *Marine pollution bulletin*, *165*, 112095.

Herlina, H., & Wissink, J. (2014). Direct numerical simulation of turbulent scalar transport across a flat surface. *Journal of Fluid Mechanics*, *744*, 217–249.

Homann, H., & Bec, J. (2010). Finite-size effects in the dynamics of neutrally buoyant particles in turbulent flow. *Journal of Fluid Mechanics*, *651*, 81–91.

Hunt, J., & Graham, J. (1978). Free-stream turbulence near plane boundaries. *Journal of Fluid Mechanics*, *84*(2), 209–235.

Ishihara, T., Kaneda, Y., Yokokawa, M., Itakura, K., & Uno, A. (2007). Small-scale statistics in high-resolution direct numerical simulation of turbulence: Reynolds number dependence of one-point velocity gradient statistics. *Journal of Fluid Mechanics*, *592*, 335–366.

Isobe, A., Kubo, K., Tamura, Y., Nakashima, E., & Fujii, N. (2014). Selective transport of microplastics and mesoplastics by drifting in coastal waters. *Marine pollution bulletin*, *89*(1-2), 324–330.

Jambeck, J. R., Geyer, R., Wilcox, C., Siegler, T. R., Perryman, M., Andrady, A., ... Law, K. L. (2015). Plastic waste inputs from land into the ocean. *Science*, *347*(6223), 768–771.

Ji, B., Song, Q., & Yao, Q. (2018). Limit for small spheres to float by dynamic analysis. *Langmuir*, *34*(34), 10163–10168.

Jin, T., & Liao, Q. (2019). Application of large scale piv in river surface turbulence measurements and water depth estimation. *Flow Measurement and Instrumentation*, *67*, 142–152.

Johnson, P. L. (2020). Energy transfer from large to small scales in turbulence by multiscale nonlinear strain and vorticity interactions. *Physical Review Letters*, *124*(10), 104501.

Jung, J., Yeo, K., & Lee, C. (2008). Behavior of heavy particles in isotropic turbulence. *Physical Review E*, *77*(1), 016307.

Koh, P., Hao, F., Smith, L., Chau, T., & Bruckard, W. (2009). The effect of particle shape and hydrophobicity in flotation. *International Journal of Mineral Processing*, *93*(2), 128–134.

Kolmogorov, A. N. (1941). The local structure of turbulence in incompressible viscous fluid for very large reynolds numbers. *Proceedings of the URSS Academy of Sciences*, *30*, 301–305.

Kraichnan, R. H. (1967). Inertial ranges in two-dimensional turbulence. *The Physics of Fluids*, *10*(7), 1417–1423.

Kukulka, T., Proskurowski, G., Morét-Ferguson, S., Meyer, D. W., & Law, K. L. (2012). The effect of wind mixing on the vertical distribution of buoyant plastic debris. *Geophysical Research Letters*, *39*(7).

Kumar, S., Gupta, R., & Banerjee, S. (1998). An experimental investigation of the characteristics of free-surface turbulence in channel flow. *Physics of Fluids*, *10*(2), 437–456.

Lebreton, L., Slat, B., Ferrari, F., Sainte-Rose, B., Aitken, J., Marthouse, R., ... Reisser, J. (2018). Evidence that the great pacific garbage patch is rapidly accumulating plastic. *Scientific Reports*, *8*(1), 1–15.

Lenain, L., Pizzo, N., & Melville, W. K. (2019). Laboratory studies of lagrangian transport by breaking surface waves. *Journal of Fluid Mechanics*, *876*.

Li, Y., Amili, O., & Coletti, F. (2022). Experimental study of concentrated particle transport in successively bifurcating vessels. *Physical Review Fluids*, *7*(8), 083101.

Lighthill, J. (2001). *Waves in fluids*. Cambridge university press.

Liu, W.-C., Chen, W.-B., & Hsu, M.-H. (2011). Using a three-dimensional particle-tracking model to estimate the residence time and age of water in a tidal estuary. *Computers & Geosciences*, *37*(8), 1148–1161.

Liu, W.-C., Lu, C.-H., & Huang, W.-C. (2021). Large-scale particle image velocimetry to measure streamflow from videos recorded from unmanned aerial vehicle and fixed imaging system. *Remote Sensing*, *13*(14), 2661.

Lovecchio, S., Marchioli, C., & Soldati, A. (2013). Time persistence of floating-particle clusters in free-surface turbulence. *Physical Review E*, *88*(3), 033003.

Lucci, F., Ferrante, A., & Elghobashi, S. (2010). Modulation of isotropic turbulence by particles of taylor length-scale size. *Journal of Fluid Mechanics*, *650*, 5–55.

Machicoane, N., & Volk, R. (2016). Lagrangian velocity and acceleration correlations of large inertial particles in a closed turbulent flow. *Physics of Fluids*, *28*(3), 035113.

Magnaudet, J. (2003). High-reynolds-number turbulence in a shear-free boundary layer: revisiting the hunt–graham theory. *Journal of Fluid Mechanics*, *484*, 167–196.

McDonald, R. R., & Nelson, J. M. (2021). A lagrangian particle-tracking approach to modelling larval drift in rivers. *Journal of Ecohydraulics*, *6*(1), 17–35.

McKenna, S., & McGillis, W. (2004). The role of free-surface turbulence and surfactants in air–water gas transfer. *International Journal of Heat and Mass Transfer*, *47*(3), 539–553.

Meijer, L. J., van Emmerik, T., van der Ent, R., Schmidt, C., & Lebreton, L. (2021). More than 1000 rivers account for 80% of global riverine plastic emissions into the ocean. *Science Advances*, *7*(18), 5803.

Mendez, M., Raiola, M., Masullo, A., Discetti, S., Ianiro, A., Theunissen, R., & Buchlin, J.-M. (2017). Pod-based background removal for particle image velocimetry. *Experimental Thermal and Fluid Science*, *80*, 181–192.

Miozzi, M., Lalli, F., & Romano, G. (2010). Experimental investigation of a free-surface turbulent jet with coanda effect. *Experiments in Fluids*, *49*(1), 341–353.

Miozzi, M., & Romano, G. P. (2020). Propagation of perturbations and meandering in a free surface shallow water jet. *Experiments in Fluids*, *61*(9), 1–18.

Moog, D. B., & Jirka, G. H. (1999). Air-water gas transfer in uniform channel flow. *Journal of Hydraulic Engineering*, *125*(1), 3–10.

Mordant, N., Lévêque, E., & Pinton, J.-F. (2004). Experimental and numerical study of the lagrangian dynamics of high reynolds turbulence. *New Journal of Physics*, *6*(1), 116.

Nakagawa, H., & Nezu, I. (1981). Structure of space-time correlations of bursting phenomena in an open-channel flow. *Journal of Fluid Mechanics*, *104*, 1–43.

Nemes, A., Dasari, T., Hong, J., Guala, M., & Coletti, F. (2017). Snowflakes in the atmospheric surface layer: observation of particle–turbulence dynamics. *Journal of Fluid Mechanics*, *814*, 592–613.

Nezu, I., Nakagawa, H., & Jirka, G. H. (1994). Turbulence in open-channel flows. *Journal of Hydraulic Engineering*, *120*(10), 1235–1237.

Nikora, V., Nokes, R., Veale, W., Davidson, M., & Jirka, G. (2007). Large-scale turbulent structure of uniform shallow free-surface flows. *Environmental Fluid Mechanics*, *7*(2), 159–172.

Ourmieres, Y., Mansui, J., Molcard, A., Galgani, F., & Poitou, I. (2018). The boundary current role on the transport and stranding of floating marine litter: the french riviera case. *Continental Shelf Research*, *155*, 11–20.

Pan, Y., & Banerjee, S. (1995). A numerical study of free-surface turbulence in channel flow. *Physics of Fluids*, *7*(7), 1649–1664.

Park, I., Seo, I. W., Kim, Y. D., & Han, E. J. (2017). Turbulent mixing of floating pollutants at the surface of the river. *Journal of Hydraulic Engineering*, *143*(8), 04017019.

Parsa, S., & Voth, G. A. (2014). Inertial range scaling in rotations of long rods in turbulence. *Physical Review Letters*, *112*(2), 024501.

Parsheh, M., Sotiropoulos, F., & Porté-Agel, F. (2010). Estimation of power spectra of acoustic-doppler velocimetry data contaminated with intermittent spikes. *Journal of Hydraulic Engineering*, *136*(6), 368–378.

Pope, S. B. (2000). *Turbulent flows*. Cambridge university press.

Raffel, M., Willert, C. E., Scarano, F., Kähler, C. J., Wereley, S. T., & Kompenhans, J. (2018). Image evaluation methods for piv. In *Particle image velocimetry* (pp. 145–202). Springer.

Rashidi, M., & Banerjee, S. (1988). Turbulence structure in free-surface channel flows. *The Physics of Fluids*, *31*(9), 2491–2503.

Raymond, P. A., Zappa, C. J., Butman, D., Bott, T. L., Potter, J., Mulholland, P., ... Newbold, D. (2012). Scaling the gas transfer velocity and hydraulic geometry in streams and small rivers. *Limnology and Oceanography: Fluids and Environments*, *2*(1), 41–53.

Rutherford, J. C. (1994). *River mixing*. Wiley.

Saddoughi, S. G., & Veeravalli, S. V. (1994). Local isotropy in turbulent boundary layers at high reynolds number. *Journal of Fluid Mechanics*, *268*, 333–372.

Sawford, B. (1991). Reynolds number effects in lagrangian stochastic models of turbulent dispersion. *Physics of Fluids A: Fluid Dynamics*, *3*(6), 1577–1586.

Shen, L., & Yue, D. K. (2001). Large-eddy simulation of free-surface turbulence. *Journal of Fluid Mechanics*, *440*, 75–116.

Shen, L., Zhang, X., Yue, D. K., & Triantafyllou, G. S. (1999). The surface layer for free-surface turbulent flows. *Journal of Fluid Mechanics*, *386*, 167–212.

Shin, M., & Koch, D. L. (2005). Rotational and translational dispersion of fibres in isotropic turbulent flows. *Journal of Fluid Mechanics*, *540*, 143–173.

Squires, K. D., & Eaton, J. K. (1991). Measurements of particle dispersion obtained from direct numerical simulations of isotropic turbulence. *Journal of Fluid Mechanics*, *226*, 1–35.

Stocchino, A., Besio, G., Angiolani, S., & Brocchini, M. (2011). Lagrangian mixing in straight compound channels. *Journal of Fluid Mechanics*, *675*, 168–198.

Stocchino, A., De Leo, F., & Besio, G. (2019). Sea waves transport of inertial micro-plastics: Mathematical model and applications. *Journal of Marine Science and Engineering*, *7*(12), 467.

Tauro, F., Petroselli, A., Porfiri, M., Giandomenico, L., Bernardi, G., Mele, F., ... Grimaldi, S. (2016). A novel permanent gauge-cam station for surface-flow observations on the tiber river. *Geoscientific Instrumentation, Methods and Data Systems*, *5*(1), 241–251.

Tauro, F., Piscopia, R., & Grimaldi, S. (2019). Ptv-stream: A simplified particle tracking velocimetry framework for stream surface flow monitoring. *Catena*, *172*, 378–386.

Taylor, G. I. (1921). Diffusion by continuous movements. *Proceedings of the London Mathematical Society*, *2*(1), 196–212.

Tennekes, H., & Lumley, J. L. (1972). *A first course in turbulence*. MIT press.

Toschi, F., & Bodenschatz, E. (2009). Lagrangian properties of particles in turbulence. *Annual Review of Fluid Mechanics*, *41*, 375–404.

Turney, D. E., & Banerjee, S. (2013). Air–water gas transfer and near-surface motions. *Journal of Fluid Mechanics*, *733*, 588–624.

Uhlmann, M., & Chouippe, A. (2017). Clustering and preferential concentration of finite-size particles in forced homogeneous-isotropic turbulence. *Journal of fluid mechanics*, *812*, 991–1023.

Uijttewaal, W., & Booij, R. (2000). Effects of shallowness on the development of free-surface mixing layers. *Physics of Fluids*, *12*(2), 392–402.

Ulseth, A. J., Hall, R. O., Boix Canadell, M., Madinger, H. L., Niayifar, A., & Battin, T. J. (2019). Distinct air–water gas exchange regimes in low-and high-energy streams. *Nature Geoscience*, *12*(4), 259–263.

Valero, D., Belay, B. S., Moreno-Rodenas, A., Kramer, M., & Franca, M. J. (2022). The key role of surface tension in the transport and quantification of plastic pollution in rivers. *Water Research*, *226*, 119078.

van den Bremer, T. S., & Breivik, Ø. (2018). Stokes drift. *Philosophical Transactions of the Royal Society A: Mathematical, Physical and Engineering Sciences*, *376*(2111), 20170104.

van Emmerik, T., & Schwarz, A. (2020). Plastic debris in rivers. *Wiley Interdisciplinary Reviews: Water*, *7*(1), e1398.

van Sebille, E., Aliani, S., Law, K. L., Maximenko, N., Alsina, J. M., Bagaev, A., ... Wichmann, D. (2020). The physical oceanography of the transport of floating marine debris. *Environmental Research Letters*, *15*(2), 023003.

van Sebille, E., Griffies, S. M., Abernathey, R., Adams, T. P., Berloff, P., Biastoch, A., ... Zika, J. D. (2018). Lagrangian ocean analysis: Fundamentals and practices. *Ocean Modelling*, *121*, 49-75.

van Sebille, E., Wilcox, C., Lebreton, L., Maximenko, N., Hardesty, B. D., van Franeker, J. A., ... Law, K. L. (2015). A global inventory of small floating plastic debris. *Environmental Research Letters*, *10*(12), 124006.

Vella, D., & Mahadevan, L. (2005). The "cheerios effect". *American Journal of Physics*, *73*(9), 817–825.

Voth, G. A., La Porta, A., Crawford, A. M., Alexander, J., & Bodenschatz, E. (2002). Measurement of particle accelerations in fully developed turbulence. *Journal of Fluid Mechanics*, *469*, 121–160.

Voth, G. A., & Soldati, A. (2017). Anisotropic particles in turbulence. *Annual Review of Fluid Mechanics*, *49*(1), 249–276.

Wang, L.-P., & Maxey, M. R. (1993). Settling velocity and concentration distribution of heavy particles in homogeneous isotropic turbulence. *Journal of fluid mechanics*, *256*, 27–68.

Weitbrecht, V., Kühn, G., & Jirka, G. (2002). Large scale piv-measurements at the surface of shallow water flows. *Flow Measurement and Instrumentation*, *13*(5-6), 237–245.

Zambianchi, E., Iermano, I., Suaria, G., & Aliani, S. (2014). Marine litter in the mediter-

995 ranean sea: an oceanographic perspective. In *Marine litter in the mediterranean and*
996 *black seas ciesm workshop monograph* (pp. 31–41).
997 Zhang, C., Shen, L., & Yue, D. K. (1999). The mechanism of vortex connection at a free
998 surface. *Journal of Fluid Mechanics*, *384*, 207–241.
999 Zhang, E., Stocchino, A., De Leo, A., & Fang, J. K.-H. (2022). Performance assessment of
1000 bubbles barriers for microplastic remediation. *Science of the Total Environment*, *844*,
1001 157027.
1002 Zhang, H. (2017). Transport of microplastics in coastal seas. *Estuarine, Coastal and Shelf*
1003 *Science*, *199*, 74–86.
1004 Zhang, Z. (2000). A flexible new technique for camera calibration. *IEEE Transactions on*
1005 *pattern analysis and machine intelligence*, *22*(11), 1330–1334.